Advanced Materials Science and Technology Vol 7 Issue 1 2025

Original Research Article

Open Access

Omniscient Pte.Ltd.

Influence of the Addition of Niobium Pentoxide on the Structural Properties of Hydroxyapatite

José Adauto da Cruz[1,*], Rodrigo Camilo[1], Stephen Rathinaraj Benjamin[2,*], Rogério Ribeiro Pezarini[3], Paulo Maria de Oliveira Silva[4], Antonio Jefferson Mangueira Sales[4] and Manuel Pedro Fernandes Graça[5]

[1] Department of Environment – State University of Maringá, Umuarama, PR, 87506-370, Brazil.

[2] Behavioral Neuroscience Laboratory, Drug Research and Development Center (NPDM), Department of Physiology and Pharmacology, Federal University of Ceará (UFC), Coronel Nunes de Melo 1127, Porangabussu, Fortaleza, Ceará, 60430-270, Brazil.

[3] Federal Institute of Paraná - R. Cariris, Nº 750 - Bairro Santa Bárbara, Capanema, PR, 85760-000, Brazil.

[4] Telecommunications and Materials Science and Engineering Laboratory (LOCEM), Federal University of Ceará (UFC), Fortaleza, CE, 60455-760, Brazil.

[5] i3N-Physics department – University of Aveiro, Aveiro, 3810-193, Portugal.

***Correspondence to:** Stephen Rathinaraj Benjamin, Behavioral Neuroscience Laboratory, Drug Research and Development Center (NPDM), Department of Physiology and Pharmacology, Federal University of Ceará (UFC), Coronel Nunes de Melo 1127, Porangabussu, Fortaleza, Ceará, 60430-270, Brazil, Email: steaje@gmail.com.

Abstract: The study focused on investigating the properties of composites made from natural hydroxyapatite (HAp, $Ca_{10}(PO_4)_6(OH)_2$) sourced from tilapia fish bones (*Oreochromis niloticus*) and niobium pentoxide (PNb, Nb_2O_5). The effects of PNb concentration and sintering temperature were examined. Composites were created using a constant pressure of 450 MPa following the formula (100-x)HAp + (x)PNb, with x varying in increments of 10%, and then sintered at temperatures ranging from 700 to 1300 °C. X-ray diffraction (XRD) analysis showed the formation of new phases based on the PNb concentration and temperature. Rietveld refinement confirmed a strong fit with experimental data, supporting the accuracy of the model parameters. Fourier Transform Infrared Spectroscopy with Photoacoustic Detection (FTIR-PAS) revealed the disappearance of the OH^- functional group at 3572 cm^{-1}. Raman spectroscopy results were consistent with XRD findings. Scanning Electron Microscopy (SEM) showed complex microstructures influenced by composition, sintering temperature, and phase interactions, with liquid-phase sintering contributing to microstructural changes. Energy Dispersive X-ray Spectroscopy (EDS) provided semiquantitative analysis, detecting the primary elements Ca, P, and Nb, along with smaller amounts of Mg and Na. The Vickers Hardness (VH) measurements indicated that PNb concentration significantly affects the mechanical properties of the composite. The study suggests that HAp/PNb composites, influenced by temperature and PNb concentration, hold great potential for use in orthopedic and dental biomaterials.

Keywords: Hydroxyapatite; Niobium pentoxide; Biomaterials; Rietveld; Vickers Microhardness.

1. Introduction

The development of advanced biomaterials for medical applications, particularly in orthopedic and dental fields, has gained significant attention in recent years[1]. Among these materials, hydroxyapatite (HAp), a naturally occurring calcium phosphate with the chemical formula $Ca_{10}(PO_4)_6(OH)_2$, has emerged as a leading candidate due to its biocompatibility, bioactivity, and structural similarity to human bone mineral[2]. Hydroxyapatite is widely used in bone grafts, coatings for dental implants, and other applications where bone regeneration and integration are required. However, pure HAp has relatively low mechanical strength and brittleness, limiting its direct application in load-bearing implants[3].To overcome these limitations, research has focused on enhancing the physical and mechanical properties of HAp through the development of composite materials. One promising approach is reinforcing the HAp matrix with various additives, such as metals, ceramics, and polymers. In this context, niobium pentoxide (Nb_2O_5) has been identified as a potential reinforcing agent for HAp composites due to its excellent biocompatibility, corrosion resistance, and non-toxicity. Niobium pentoxide, PNb when incorporated into HAp, has shown potential in improving the composite's mechanical properties, making it suitable for a broader range of biomedical applications[4].

Despite the promising properties of HAp/Nb_2O_5 composites, there is limited research on how varying the concentration of Nb_2O_5 and the sintering temperature affects the composite's overall properties. The present study aims to fill this gap by systematically investigating the effects of different concentrations of niobium pentoxide and varying sintering temperatures on the physical, structural, and mechanical properties of HAp/PNb composites. The chemical ionization process and powder metallurgy techniques will be employed to synthesize the composites with varying proportions of HAp and PNb[5,6]. Previous studies have indicated that adding metal oxides such as niobium oxide to HAp can enhance its use in bone repair applications. For instance, Tamai et al.[7] and Fathi et al.[8] demonstrated that niobium oxide could be a reinforcing material to improve bone repair efficiency. Silva et al.[9] explored various applications of niobium oxide in medicine, highlighting its potential in enhancing the calcification process of human osteoblasts. Additional studies have shown that composites derived from natural sources of HAp, such as animal bones, could benefit from reinforcement with materials like niobium oxide to improve mechanical properties[10–16]. These findings suggest that the inclusion of Nb_2O_5 could significantly influence the performance characteristics of HAp-based composites.

This study focuses on exploring the effects of varying Nb_2O_5 concentrations (ranging from 0% to 100% in increments of 10% by volume) and different sintering temperatures (from 700 to 1300°C) on the resulting HAp/PNb composites. The composites will be produced using powder metallurgy techniques, a method known for precisely controlling particle size distribution, homogeneity, and mechanical properties. The samples will be compacted under a constant pressure of 450 MPa to ensure uniform density and sintered under controlled atmospheric conditions.

2. Materials and Methods

The HAp used in this work was obtained in the DFI/UEM laboratories via calcination and grinding of tilapia bones (*Oreochromis niloticus*)[17] according to the procedures contained in patent PI0506242-0[18] from the same department. Niobium pentoxide was supplied by the Brazilian Company of Mines and Mining (CBMM) as a powder with a purity of around 99.5%. The material, as received, after analysis by X-ray diffraction (XRD), showed polymorphic forms[19,20] that, after heat treatment at 1100 °C for 3 h were eliminated, resulting in the H-Nb_2O_5 phase, monoclinic system and space group P12/m1 (10) according to the Joint Committee on Powder Diffraction Standards (JCPDS) 037-1468 and Inorganic Crystal Structure Data Base (ICSD) standard form. The materials were ground in Retsch planetary ball mills model PM100, high energy mill Haan-Germany for 3 h at 300 rpm with 10 min stops every 1 h (to reduce heating and avoid overheating) in ambient air.

Particle size distribution analysis was conducted using Dynamic Light Scattering (DLS) equipment from Malvern Instruments Ltd. with serial number MAL 107- 8015. Prior to analysis, the powder particles were suspended in acetone (dispersing medium) and sonicated for 5 minutes to minimize particle aggregation effects.

For XRD analysis, a Shimadzu XRD - 7000 diffractometer with CuKα radiation (λ=0.15418 nm) and Bragg-Brentano geometry operating at 40 kV, 30 mA was utilized.

Spectroscopic techniques, particularly the Fourier Transform Infrared Spectroscopy with Photoacoustic Detection (FTIR-PAS) technique, were performed using a VERTEX 70/70v Bruker Corporation spectrophotometer from Germany with PAS accessory for analysis of powder samples. Raman spectroscopy measurements were carried out for analyzing HAp and PNb precursors using a Bruker Confocal Raman micro spectrometer model SENTERRA.

The equipment employed 20 x optical magnifications, with an excitation laser featuring a wavelength of 532 nm, power of 20 mW, and 20 scans, each acquired for 3 seconds in each exposure. Samples for Scanning Electron Microscopy (SEM) analyses were coated with a conductive gold film using a sputtering process on a Shimadzu metallizer (IC-50 Ion Coater) and observed using an FEI QUANTA 250.5 microscope at 30 kV.

TGA (Thermo Gravimetric Analysis) and DTA (Differential Thermal Analysis) thermal analysis was conducted using a Simultaneous Thermo Analysis (STA) 409 PC (Selb, Germany) model Netzsch. The equipment is equipped to measure DTA curves simultaneously with TGA and includes a microbalance, an oven, thermocouples, and a gas flow system. The sample measurements were conducted by placing the samples in alumina crucibles with a heating and cooling rate of 10 °C/min in an atmosphere containing 70% nitrogen gas and 30% oxygen gas, with a 50 ml/min flow rate. For dilatometry, a commercial NETZSCH DIL (Dilatometer) 402 PC-Horizontal pushrod dilatometer was used, in which the sample is placed inside an oven and pressed by a rod (Pushrod). Cylindrical-shaped green pieces with dimensions of 25 mm in length and 5 mm in diameter were produced for these tests.

The mechanical property was evaluated using only the Vickers microhardness technique. This was measured on a Vickers Microhardness Digital Low Load Display, Hardness Tester, Model HVS-5, Serial Number 0040. Indentations were performed using a 1000 g load for a period of 15 s. The Vickers hardness (HV) value was obtained by averaging 12 indentations in each sample. For these analyses, the samples were sanded and polished in a Panambra model DP9 polisher with 400 to 1200 # sandpaper and final polishing with diamond paste 0.1 to 0.3 μm.

2.1. Composition of hydroxyapatite with niobium pentoxide

2.1.1. Mixing, homogenization and conformation

The (100-x)HAp+(x)PNb composite, with x ranging from 0 to 100% in 10% intervals, was obtained using powder metallurgy[21] and high-energy milling[22] techniques. As for the nomenclature used to designate the composites, the following form was used for simplification purposes: H9N1, mean, 90% HAp and 10% PNb by vol.%, H8N2, 80% HAp and 20% PNb by vol. % and so on, in the composition, from the equation (100-x)HAp+(x)PNb. The precursors were mixed in the selected proportions, and manually homogenized for 15 min followed by milling. Then, the powder composites were formed into a cylindrical shape with dimensions of approximately ~10 mm in diameter (D) and ~2.00 mm in thickness (h) in a rigid matrix of VC 131 steel already submitted to tempering to increase its hardness. Samples were produced at a pressure of 450 MPa on a Metal PEM press, PHP-30 TONs.

2.1.2. Sintering

The composites were sintered in a tubular furnace with temperature control and room atmosphere. Sintering was carried out at temperatures ranging from 700 to 1300 °C for 2 hours in one atmosphere. The process included cooling by thermal inertia after the furnace automatically shut down.

2.2. Physical properties

2.2.1. Dimensional variation

The dimensional variation comprising linear retraction or expansion was obtained by comparing the diameter measurement of the green sample (D_v) and the measurement after sintering (D_s). Measurements were performed with a JOMARCA digital caliper Ref. 0205509-Brasil, with a resolution of 0.01 mm. The resulting dimensional variation value corresponds to the mean value of six samples and was calculated from equation (1):

$$VDI(\%) = \frac{(D_s - D_v)}{D_v}.100 \qquad (1)$$

in which:

VDI (%): dimensional variation;

D_s: final dimension (diameter of the sintered part);

D_v: initial dimension (green part diameter).

2.2.2. Density

The density of the sintered samples was measured by the immersion method based on the Archimedes principle, ASTM C373-88[23]. They were dried for 12 hours in an oven at 110 °C and then their masses were measured on a digital scale Shimadzu AUW220D (Kyoto, Japan) with 5 (five) decimal places using the Specific Gravity Measurement Kit. Then, they were accommodated on a tray and placed inside a chamber, where a vacuum was created at 10^{-2} Torr for 2 hours. Subsequently, the tray was flooded with distilled water through a funnel attached to the chamber. For measurements of impregnated and immersed masses, a thermalization time of 30 minutes at room temperature was expected. Density and porosity values also correspond to the average value of measurements performed on 6 (six) samples. Density was calculated according to equation (2):

$$\rho_S = \frac{m_S}{m_{imp} - m_e} \rho_{water} \tag{2}$$

in which:

ρ_s: density of the sintered sample;

ρ_{water}: density of water at the temperature at which the measurement was performed;

m_s: mass of the sintered and dried sample;

m_{imp}: sample mass impregnated with water;

m_e: mass of the sample under the buoyancy of the water.

2.2.3. Porosity

The porosity of the sintered composites was evaluated using equation (3):

$$\gamma(\%) = \frac{m_{imp} - m_s}{m_{imp} - m_e}.100 \tag{3}$$

in which:

$\gamma(\%)$ open porosity and percentage by volume;

2.3. Mechanical property

The mechanical property was evaluated using only the Vickers microhardness technique. This was measured on a Vickers Digital Displaylow Load Micrometer, Hardness Tester, Model HVS-5, Serial Number 0040. Indentations were performed using a 1000 g load for a period of 15 s. The Vickers hardness value was obtained by averaging 12 indentations in each sample. For these analyses, the samples were sanded and polished in a Panambra polisher, model DP9, with 400 to 1200# grit sieves and final polishing with diamond paste with 0.1 to 0.3 μm grit.

3. Results and Discussion

3.1. Sinterized composite analysis (100-x)HAp + (x) PNb

3.1.1. Dimensional variation

The knowledge of the dimensional variation is of great importance for producing components obtained by powder metallurgy techniques, as this property allows estimating the dimensional accuracy for large-scale production. In this work, 170 °C were selected, in the range between 700 and 1300 °C, to evaluate the behavior of the composites (100-x)HAp+(x)PNb, mainly in the range between 1000 and 1100 °C, and select the ideal sintering temperature as a function of the percentage volume of PNb in the HAp matrix.

Figure 1(A-C) shows the effect of concentration and temperature on the composites produced. In **Figure 1(A)** from 700 to 1020 °C, for composites sintered at 700 and 800 °C, a slight expansion of around 1% is observed for all concentrations. At 900 °C, the composites with concentrations lower than and equal to 50% of PNb, present a small contraction and for higher concentrations a slight expansion. From 950 to 1020 °C, contraction is observed, with the exception of about 90% of PNb. This behavior is evidenced mainly at the temperature of 1020 °C for concentrations of up to 40% of PNb; this effect is attenuated from this concentration. The greatest shrinkage of the order of 6.65% occurs for the H6N4 composite at 1020 °C. For the temperature range between 1040 and 1090 °C, see **Figure 1 (B)** shows a retraction for all concentrations and a small expansion for the H0N10 sample. Between 40 and 70% concentrations, the highest contraction values occur, with a maximum value of approximately 9.56% for the 60% concentration of PNb at 1080 °C and expansion for the H0N10 sample, at all temperatures. In the range between 1100 and 1300 °C, see **Figure 1(C)**, contraction occurs for composites with concentrations smaller than and equal to 20%, while for concentrations of 30, 40 and 80% of PNb, there is expansion and a maximum value of 16, 54% for the H2N8 composite, sintered at a temperature of 1300 °C. At a temperature of 1100 °C, shrinkage occurs for composites with concentrations lower than and equal to 90%. The highest contraction value of 9.75% was observed for compound H4N6, for a concentration of 60% of PNb.

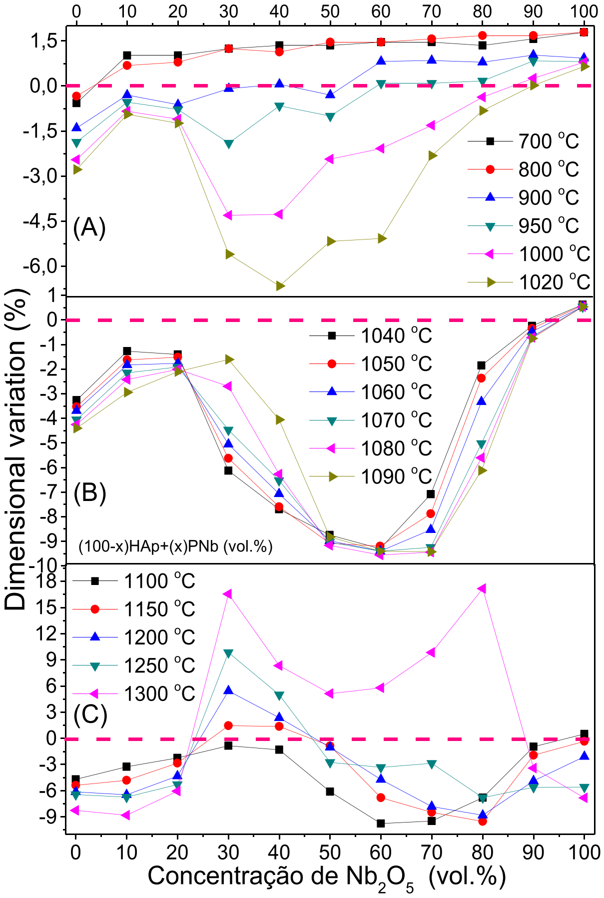

Figure 1 (A-C). Effect of sintering concentration and temperature on the dimensional variation of the precursors and composites (100-x)HAp+(x)PNb, with x = 0, 10, 20, 30, 40, 50, 60, 70, 80, 90 and 100 (vol.%).

3.1.2. Density

It is expected that the density of a material, **Figure 2(A-C)**, separated in the same temperature ranges as the previous figure, obtained by powder metallurgy techniques, reaches higher values when the dimensional variation also presents higher values due to decreased porosity. In **Figure 2(A)**, the lowest density values are observed for composites with 10% PNb concentration and sintered at temperatures of 700, 800 and 900 °C. Also for all concentrations, a progressive increase in density is observed as a function of the increase in temperature for PNb concentrations greater than 10%, except composites sintered at temperatures of 1000 and 1020 °C, in which there was a sharp increase in density with values of 3.14 and 3.43 g/cm^3, respectively, for the H4N6 composition. In the range from 1040 to 1090 °C, see **Figure 2(B)**, an increasing density increase is observed up to the concentration of 60% of PNb, which is evidenced for the temperatures of 1070, 1080 and 1090 °C in the concentration of 70% PNb or H3N7. At higher concentrations, there is a decrease in density values. In general, in the analyzed temperature range, a similar behavior is observed for all compositions, with the lowest density of 2.48 g/cm^3 observed in the H9N1 sample (1040 °C) and the highest of 3.87 g/cm^3 in the composition H3N7 (1080 °C). For the temperature range between 1100 and 1300 °C, shown in **Figure 2(C)**, the density presents a practically constant behavior, affected only by the sintering temperature, for the compositions with lower concentrations of PNb, between 10% and 20%. For concentrations between 20 and 40%, there is a decrease in density at all temperatures, with a minimum value of 2.01 g/cm^3, in the H7N3 composition sintered at

1250 °C. For PNb concentrations between 40% and 80%, an increase in density is observed, reaching a maximum value of 3.93 g/cm^3 for the sintered H2N8 composition between 1150 and 1250 °C. At concentrations greater than 80% of PNb, there is a small decrease in density values at all temperatures, being more pronounced at temperatures of 1100, 1150 and 1200 °C.

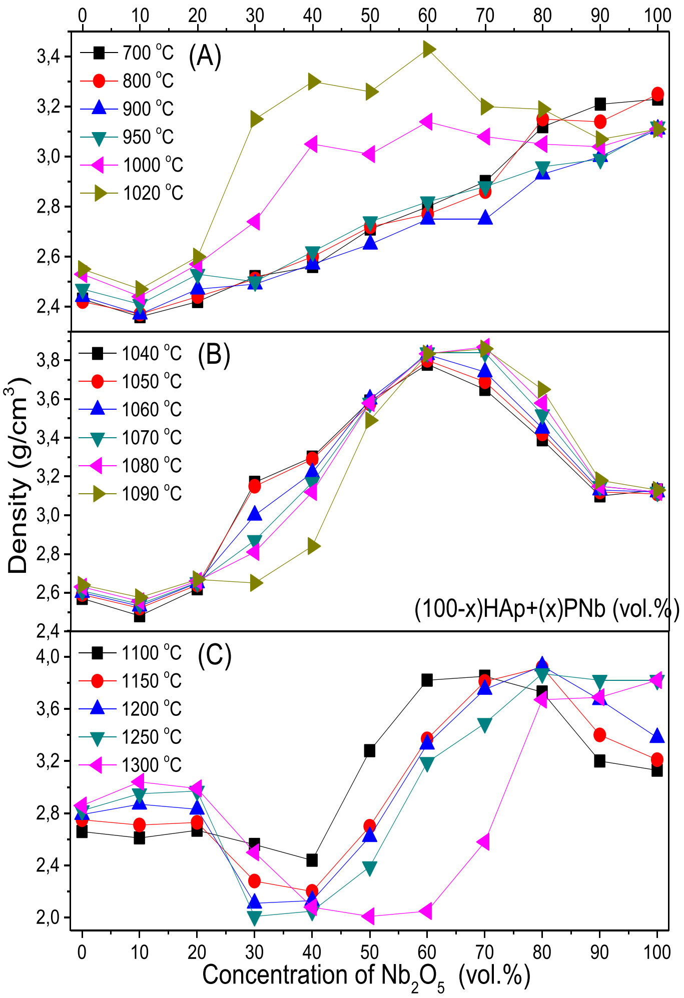

Figure 2 (A-C). Variation of density in composites (100-x)HAp+(x)PNb as a function of the temperature and concentration of the HAp and PNb precursors, with x = 0, 10, 20, 30, 40, 50, 60, 70, 80, 90 and 100 (vol.%).

3.1.3. Porosity

Figure 3(A-C) shows the results of porosity variation as a function of the respective sintering temperature and composition. In **Figure 3(A)**, the porosity at all PNb concentrations is between 11% and 33% for the temperature range between 700 and 1020 °C. At temperatures of 1000 and 1020 °C, there is a marked decrease in porosity, notably at concentrations of 30 to 60% of PNb. In the range from 1040 to 1090 °C, **Figure 3(B)** shows a porosity ranging from 13 to 23% for H8N2 and H9N1 composites. From the composition of H7N3, there is a sharp decrease in porosity reaching a value close to 4% in the composition of H4N6 sintered at 1090 °C. For higher concentrations of PNb, a gradual growth occurs, obtaining for the sample H0N10, a value around 31% at all temperatures. The porosity variation in the range of 1100 to 1300 °C is shown in **Figure 3(C)**. There is an increase in porosity up to 30 and 40% (H7N3 and H6N4) at concentrations, and at higher concentrations, there is a marked decrease in the H2N8 composition. For higher concentrations, a small increase in porosity occurs. In the analyzed temperature range, the H6N4 composition showed the highest porosity (44.8%) at 1250 °C, while the lowest porosity, 4.35%, occurred for the H4N6 composite at 1100 °C.

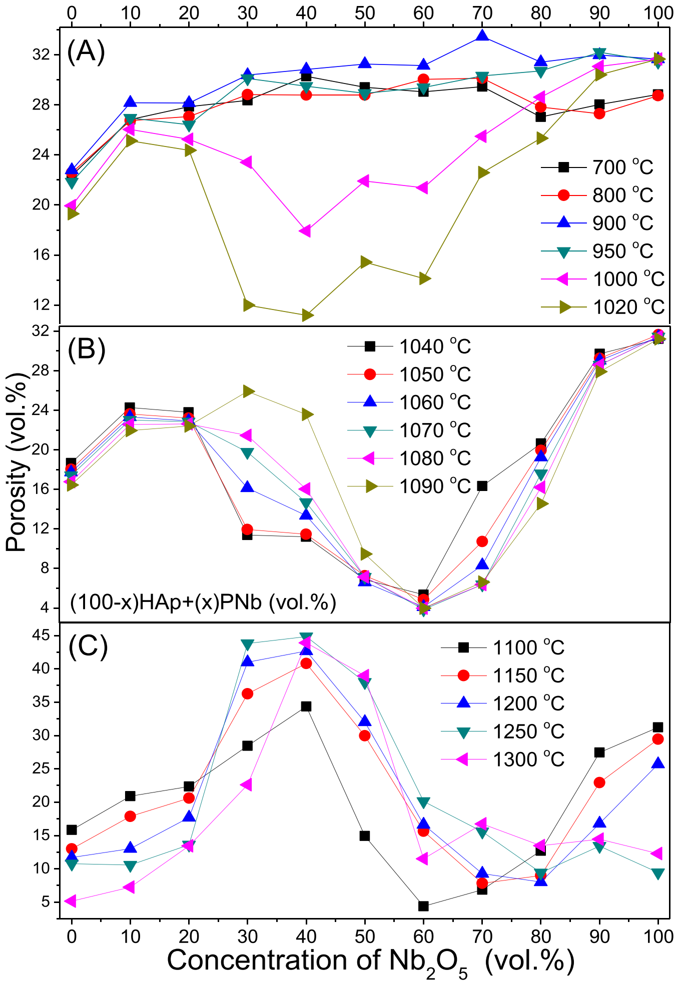

Figure 3 (A-C). Porosity variation in composites (100-x)HAp+(x)PNb as a function of the sintering temperature and the concentration of the HAp and PNb precursors, with x = 0, 10, 20, 30, 40, 50, 60, 70, 80 , 90 and 100 (vol.%).

3.1.4. Final remarks on physical properties

In the composites analyzed in terms of dimensional variation, density and porosity, there is a significant variation in these quantities since both the concentration and the sintering temperature influence the properties of the composites produced. The increase in densification is related to the greater sinterability of the material in view of the increase in the sintering temperature and also in the concentration of the constituent materials. It is observed, for example, that for the same temperature, both the increase and the decrease in density occur as a function of the percentage variation of the HAp and PNb precursors, which is an important characteristic of the composite. During sintering, depending on the characteristics of the raw materials and the concentrations used, sintering may occur in the liquid phase and as a consequence of the decrease in the temperature of the melting point of the composite, compared to the constituent materials, which allows to obtain values higher for density at lower temperatures[24].

3.2. X-Ray Diffraction Analysis of Sintered Composites

Figure 4(A-C) and **(D-F)** shows the diffractograms of the sintered composites as a function of the sintering temperature and for some concentrations with x = 10, 30, 40, 50, 60 and 90 (vol%). For the study, 14 temperatures were selected. After the sintering process, the samples were powdered for XRD analysis. At the bottom of the figures, the diffractograms of the HAp and PNb precursors are presented. The analysis of the diffractograms of the composites shows the decomposition of the HAp and PNb precursors, except for the H9N1 and H1N9 composites, in which small residual amounts of H10N0 and H0N10 are observed respectively and the formation of new phases: (*) β-TCP beta phosphate tricalcium ($Ca_3(PO_4)_2$); (●) fersmite ($CaNb_2O_6$); (♦) niobium phosphorus oxide (PNb_9O_{25}) and (+) dicalcium diniobate oxide ($Ca_2Nb_2O_7$), corresponding to standard forms JCPDS 009-0169, 039-1392, 081-1304 and 070-2006, respectively.

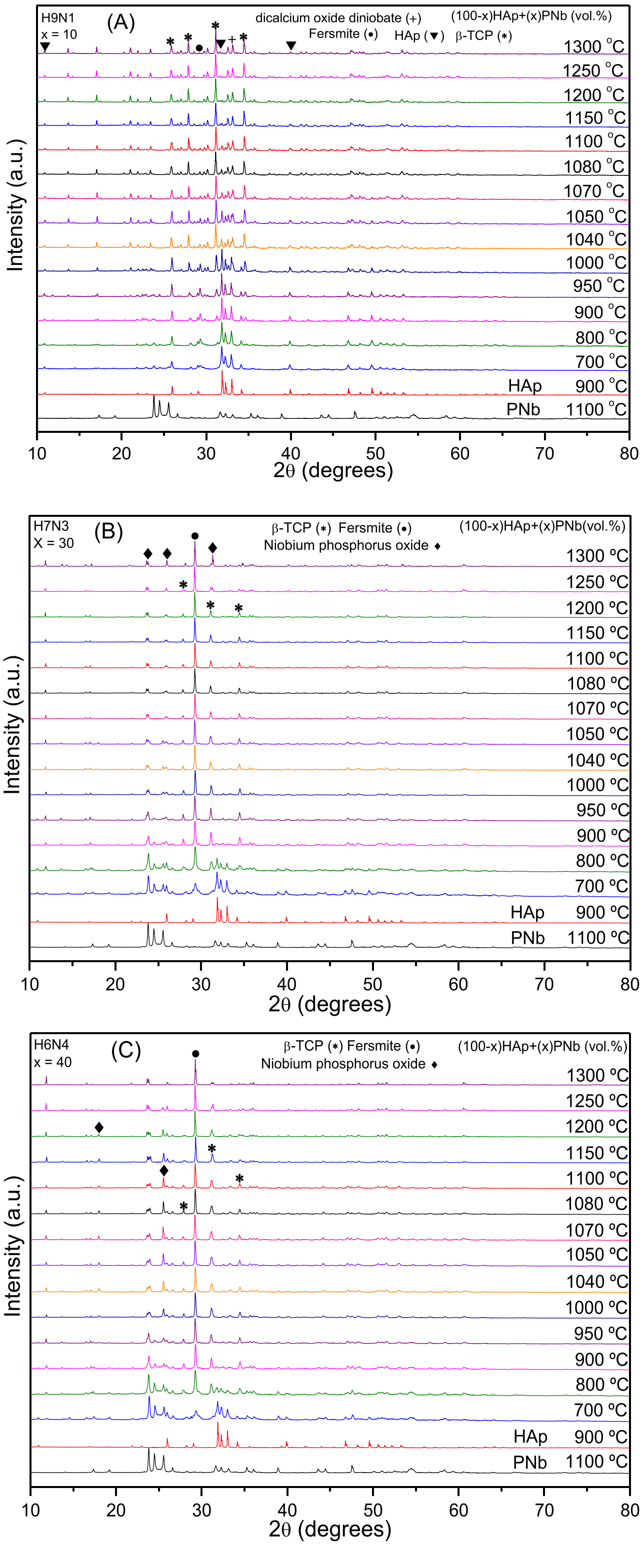

Figure 4 (A-C). X-ray diffractograms of the composites (100-x)HAp+(x)PNb, for x = 10 (A), 30 (B) and 40% of PNb (C) in vol.%, as a function of the sintering temperature.

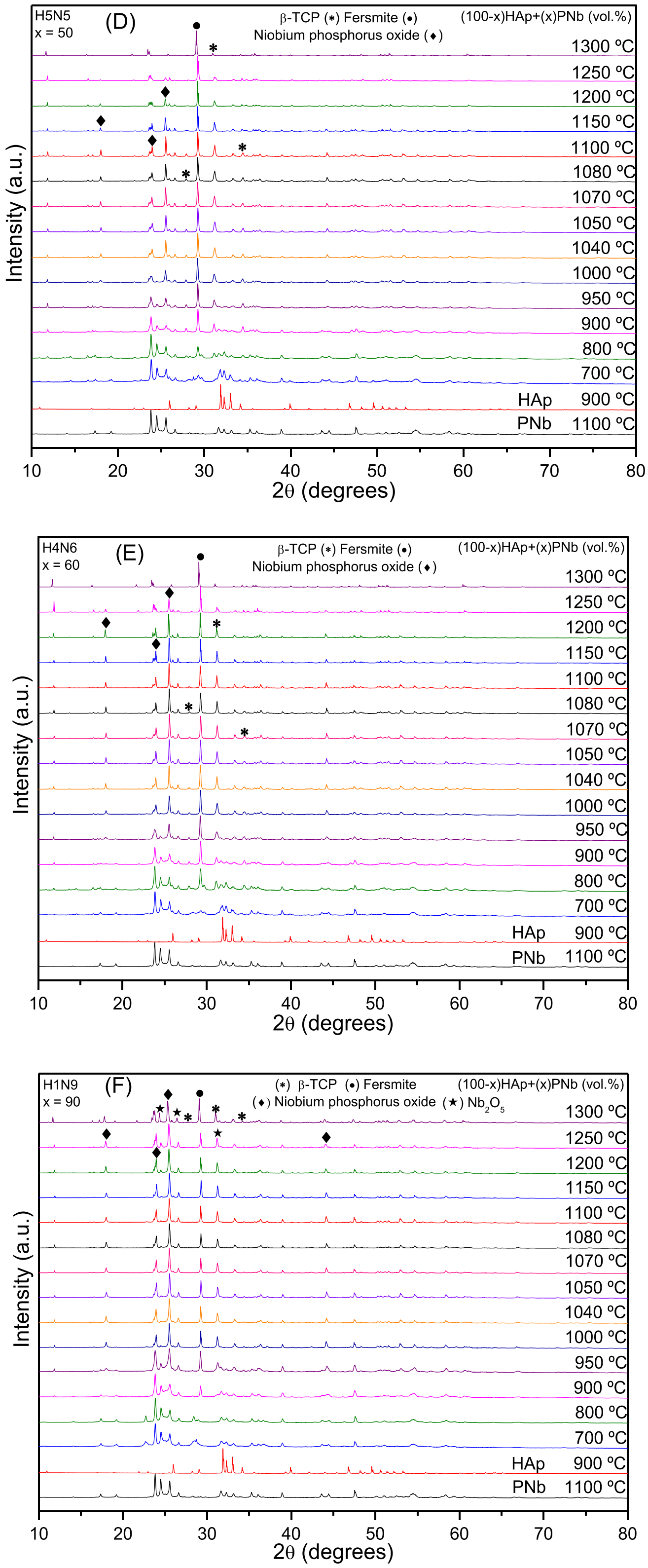

Figure 4 (D-F). (cont.) X-ray diffractograms of the composite (100-x)HAp+(x)PNb, with x = 50 (D), 60 (E) and 90% of PNb (F) in (vol.%), as a function of the sintering temperature.

Table 1 shows the temperature ranges for the formation of the structural phase observed in the diffractograms of the composites as a function of the sintering temperature and the concentration of the PNb reinforcement, which indicate the possible beginning of the appearance of the phase in the composites studied as a result of the decomposition of the composites precursor phases that occur during sintering. It is observed that (*) the β-TCP and (●) fersmite phases are present in all compositions between 10% and 90% and are detected in some concentrations at a temperature of 700 °C, and may even occur at lower temperatures[24]. The phase (♦) of niobium phosphorus oxide (PNb_9O_{25}) is only observed in concentrations equal to and greater than 30% of Nb_2O_5 and its formation temperature depends on the concentration of PNb. The ($Ca_2Nb_2O_7$) (+) phase is only observed for the composition with H9N1 and at temperatures close to 800 °C.

Table 1. Composite phase formation temperature (100-x)HAp+(x)PNb intervals observed in the XRD analyses.

Sample	Phase(*)	Phase(●)	Phase(♦)	Phase(+)	Sample	Phase(*)	Phase(●)	Phase(♦)	Phase(+)
	ΔT(°C)	ΔT(°C)	ΔT(°C)	ΔT(°C)		ΔT(°C)	ΔT(°C)	ΔT(°C)	ΔT(°C)
H9N1	800	700	-	900	H4N6	700	700	850	-
H8N2	700	700	-	-	H3N7	700-800	700	700	-
H7N3	700	700	1150	-	H2N8	700-800	700	700	-
H6N4	700	700	1000	-	H1N9	800-900	700	700	-
H5N5	700	700	900	-	x	x	x	x	X

Subtitle: (*) $Ca_3(PO_4)_2$, (●) $CaNb_2O_6$, (♦) PNb_9O_{25} and (+)$Ca_2Nb_2O_7$.

3.3. Analysis of Composites with Maximum Densification

In the previous topics of this work, a density variation was observed, which is related to the greater sinterability of the material due to the increase in the sintering temperature and the percentage (%) of the niobium pentoxide reinforcement [PNb, Nb_2O_5]. Thus, an increase or decrease in density may occur for the same temperature, depending on the percentage of constituent materials. **Table 2** presents the results obtained for the density of the series of composites studied as a function of the temperature of the composition. Among these composites, the (9) compositions that presented the highest density values and the precursors HAp and PNb (H10N0 and H0N10, respectively) were selected. The maximum densification temperatures are presented in **Table 2**. These compositions will then be analyzed by different techniques, such as X-ray diffraction (XRD), structural refinement (Rietveld method), infrared spectroscopy (FTIR-PAS), Raman spectroscopy, SEM /EDS and Vickers Microhardness (VH).

Table 2. Density as a function of volume (%) and sintering temperature in the precursors and composites (100-x)HAp+(x)PNb, with x = 0, 10, 20, 30, 40, 50, 60,70, 80 , 90, 100 (vol.%).

TEMP(°C)	H10N0	H9N1	H8N2	H7N3	H6N4	H5N5	H4N6	H3N7	H2N8	H1N9	H0N10
700	2,43	2,36	2,42	2,52	2,56	2,71	2,80	2,90	3,12	3,21	3,23
800	2,42	2,37	2,44	2,51	2,6	2,72	2,77	2,86	3,15	3,14	3,25
900	2,44	2,37	2,47	2,49	2,57	2,65	2,75	2,75	2,93	3,00	3,11
950	2,47	2,41	2,53	2,5	2,62	2,74	2,82	2,88	2,96	2,99	3,12
1000	2,53	2,44	2,57	2,74	3,05	3,01	3,14	3,08	3,05	3,04	3,11
1020	2,55	2,47	2,6	3,15	3,30	3,26	3,43	3,20	3,19	3,07	3,11
1040	2,57	2,48	2,62	3,17	3,30	3,58	3,78	3,65	3,39	3,1	3,13
1050	2,59	2,52	2,64	3,15	3,29	3,58	3,80	3,69	3,42	3,12	3,11
1060	2,60	2,53	2,65	3,00	3,22	3,58	3,83	3,74	3,45	3,13	3,12
1070	2,61	2,54	2,653	2,87	3,17	3,58	3,83	3,84	3,52	3,15	3,12
1080	2,63	2,56	2,66	2,81	3,12	3,59	3,83	3,85	3,58	3,15	3,12
1090	2,64	2,58	2,67	2,65	2,84	3,49	3,84	3,85	3,65	3,18	3,13
1100	2,66	2,61	2,67	2,56	2,44	3,28	3,84	3,86	3,73	3,20	3,13
1150	2,75	2,71	2,73	2,28	2,2	2,7	3,37	3,81	3,93	3,40	3,21

Continuation Table:

TEMP(°C)	H10N0	H9N1	H8N2	H7N3	H6N4	H5N5	H4N6	H3N7	H2N8	H1N9	H0N10
1200	2,79	2,87	2,83	2,11	2,13	2,62	3,33	3,75	3,92	3,67	3,38
1250	2,82	2,95	2,97	2,01	2,05	2,39	3,19	3,49	3,87	3,82	3,82
1300	2,86	3,04	2,99	2,50	2,08	2,01	2,05	2,58	3,67	3,69	3,82

3.3.1. X-ray diffraction analysis of selected DRX composites

Figure 5 shows the diffractograms of the selected composites and the HAp and PNb precursors. The diffractograms of the HAp and PNb phases, respectively, are shown at the bottom and top of **Figure 5**. For the H10N0 (HAp) sample, sintered at 1300 °C, a broad peak of low intensity centered around 2θ = 31.08º, which can be attributed to the β-TCP phase (JCPDS 009-0169), is observed according to and indicates the decomposition of HAp (dehydroxylation) at a temperature of 1300 °C. The other peaks are related to the HAp phase (JCPDS 009-0432). The diffractogram of the PNb phase corresponds to the H-Nb_2O_5 phase, according to JCPDS 037-1468. For the compositions H7N3, H6N4, H5N5, H4N6, H3N7, H2N8 and H1N9, we observed the complete decomposition of the HAp and PNb phases and the formation of phases: (*) $Ca_3(PO_4)_2$, (●) $CaNb_2O_6$ and (♦) PNb_9O_{25} , corresponding to JCPDS standard datasheets: 009-0169; 039-1392; and 081-1304, respectively. The intensity of the reflections relative to the identified phases varies according to the concentration of each composite, as can be seen in the maximum intensity peaks of each phase: β-TCP phase located around 2θ = 31.10º, fersmite around 2θ = 29.22º and niobium phosphorus oxide at approximately 2θ = 25.48º. In the composition of H9N1, four phases are observed (▼) HAp, (*) β-TCP, (●) fersmite and (+) dicalcium oxide diniobate, the latter being detected only in this composition. For the H8N2 composite, only phases (*) β-TCP and (●) Fersmite $CaNb_2O_6$ were identified. A larger study of the phases identified after sintering and the quantitative analysis of the phases by determining the mass fraction of each phase (weight fraction) will be the object of study through structural refinement by the Rietveld method[25].

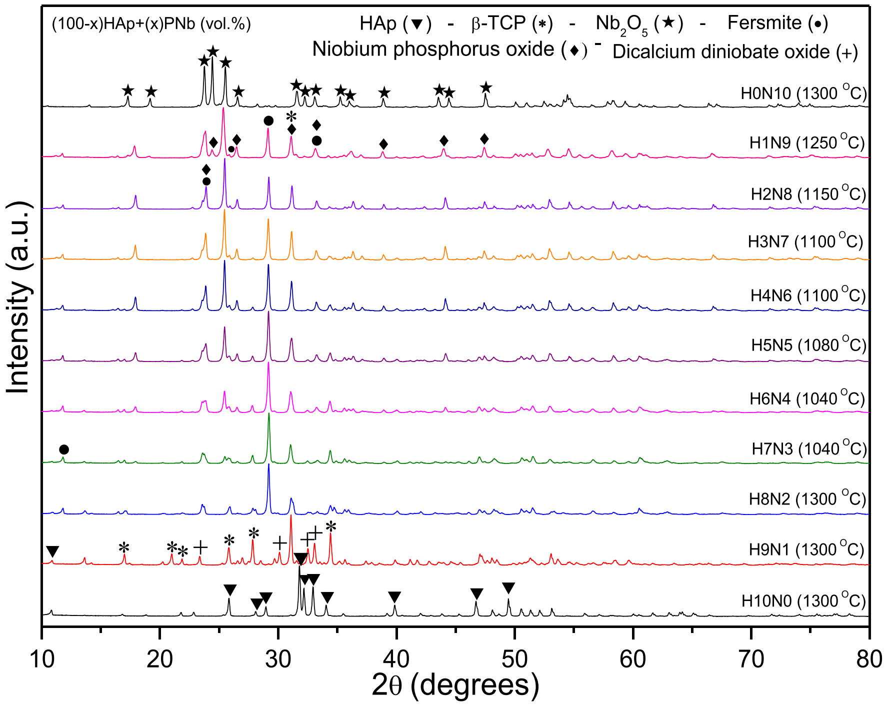

Figure 5. X-ray diffraction patterns of the selected composites and their respective sintering temperatures and precursors

3.3.2. Structural refinement by Rietveld method of selected composites

To evaluate the structural changes and quantify the percentage of each phase in the selected composites, the Rietveld method performed the structural refinement using the fullprof program. For the start of the refinement, the ICSD data sets 26-204, 29, 410782, 15208, 72683 and 6117, corresponding to the phases, (▼) $Ca_{10}(PO_4)_6(OH)_2$, (★) Nb_2O_5, (*) $Ca_3(PO_4)_2$, (●) $CaNb_2O_6$, (♦) PNb_9O_{25} and (+) $Ca_2Nb_2O_7$, respectively. The quality factors of the numerical adjustments related to the refinement of the analyzed composites are presented in **Table 3**. They indicate that the simulated pattern presented an acceptable approximation of the observed pattern; that is, the values obtained for the simulated pattern are sufficiently close to the values of the actual parameters. It is also observed, when analyzing the experimental and calculated (simulated) diffractograms, a good agreement, evidencing a correct choice of structures and initial parameters selected for refinement. The observed and calculated diffractograms, their differences and the Bragg positions are shown in **Figure 6(A-C)** and **(D-F)**, for some composites (A) H9N1, (B) H7N3, (C) H6N4, (D) H5N5, (E) H4N6 and (F) H1N9. The values of the lattice parameters, unit cell volume, density and quantitative analysis (mass fractions %) of the phases identified in the selected composites are listed in **Tables 4-9**. The analysis of the network parameters shows a small variation in relation to the JCPDS standards used to identify the phases by the comparison method. These variations are observed mainly in composites with two or more phases and are possibly related to the coexistence in the material[26].

One of the objectives of the structural refinement was the quantitative analysis of the remaining crystalline phases in the composites, as a function of the sintering temperature and PNb concentration. **Table 10** shows the percentage values (mass fraction %) of the crystalline phases observed in the selected composites and also of the precursors. The evolution of the mass fraction (% mass) of the analyzed phases can be seen in **Figure 7**. The highlighted line, the symbol (--ϴ--), is just a visual guide to indicate the temperatures at which the maximum densities were observed both for the selected composites and for HAp and PNb. The beginning of the decomposition of the (▼) HAp phase is observed, due to the used temperature of 1300 °C, due to dehydroxylation, that is, loss of OH^- ions and appearance of the (*) β-TCP phase, with quantitative percentage around 3.4%. Note also, for all composites with $x \neq 0$, the decomposition of precursors (▼) HAp) and (★) PNb and that the mass fraction (% mass) of the resulting phases depends on both temperature and composition. The highest quantitative percentage observed for phase (*) β-TCP, occurs in the compound H9N1 and, from that, with the increase in the concentration of PNb, there is a decrease in this percentage from 77.88% (H9N1) to 1.77 % in Composition of H1N9. The (●) $CaNb_2O_6$ phase is detected in the H9N1 composition and its quantitative percentage increases for the H7N3 composition from 0.9% to 41.59%. Then, it presents a continuous decrease until the H1N9 composition, with a value of 23.88%. The (♦) PNb_9O_{25} phase is observed starting from the H7N3 composite with a quantitative percentage (% in mass) of 8.09% and increases at a practically constant rate, until the H2N8 composite for the value of 63.87%, and decreases to 58.12% in the H1N9 composition. The (+) $Ca_2Nb_2O_7$ phase is only observed in the H9N1 composition with a percentage of 19.48%. In general, it is observed in the concentration of PNb reinforcement, a decrease in the quantitative percentage for the phase (*) β-TCP (more pronounced) milder for fersmite (●) $CaNb_2O_6$ and an increase for the phase niobium phosphorus oxide (♦) PNb_9O_{25}.

Table 3. Quality factors of the adjustments related to refinement by Rietveld.

composite	Quality factors of the adjustments				**composite**	Quality factors of the adjustments			
	Rp (%)	Rwp (%)	Rexp (%)	χ^2		Rp (%)	Rwp (%)	Rexp (%)	χ^2
H10N0	8,41	11,40	5,66	4,03	H4N6	6,69	8,81	4,17	4,47
H9N1	7,32	9,58	5,03	3,62	H3N7	7,04	9,40	4,40	4,55
H8N2	11,90	16,30	4,87	11,10	H2N8	7,55	10,00	3,99	6,33
H7N3	6,37	8,52	5,12	2,77	H1N9	8,41	11,10	4,56	5,96
H6N4	6,53	8,53	4,62	3,40	H0N10	13,20	17,00	6,47	6,94
H5N5	7,00	9,12	4,32	4,46	-	-	-	-	-

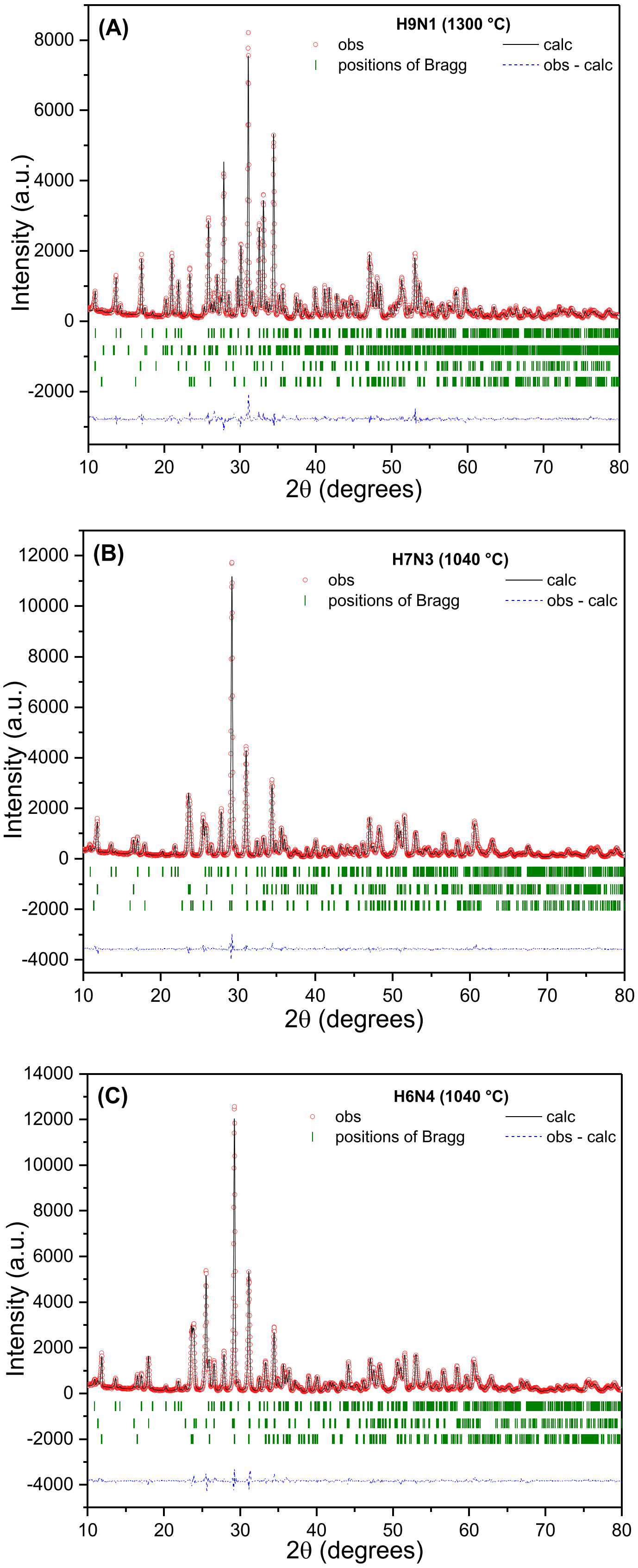

Figure 6 (A-C). Experimental and calculated diffractograms after the refinement by the Rietveld method of the sintered composites: (**A**) H9N1, (**B**) H7N3 and (**C**) H6N4.

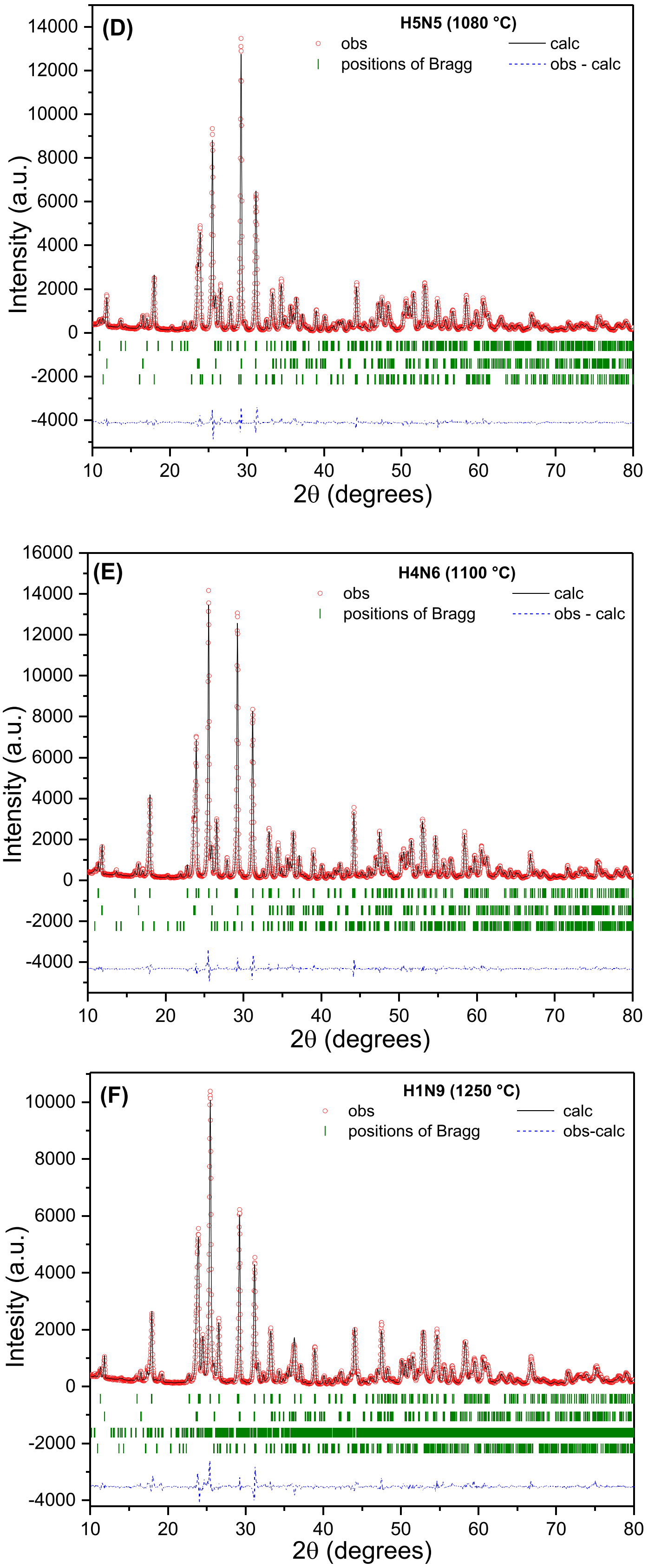

Figure 6 (D-F). (cont.) Experimental and calculated diffractograms after refinement by the Rietveld method of the sintered composites: (**D**) H5N5, (**E**) H4N6 and (**F**) H1N9.

Table 4. Parameters obtained from the refinement referring to β-TCP phase.

Phase: Beta-Phosphate Tricálcico -- β-TCP -- $Ca_3(PO_4)_2$

System: Rhombohedral - Space Group: R3c (167) -- α = β = 90° -- γ = 120°

composite	mass (%)	*a* (Å)	*b* (Å)	*c* (Å)	V(Å^3)	ρ (g/cm^3)
H10N0	3,39 (0,02)	10,420 (0,003)	10,420 (0,003)	37,36 (0,01)	3513 (2)	3,079
H9N1	77,9 (0,7)	10,4127 (0,0005)	10,4127 (0,0005)	37,34 (0,012)	3505,7 (0,3)	3,085
H8N2	67,6 (1,3)	10,3623 (0,0006)	10,3623 (0,0006)	37,222 (0,003)	3461,3 (0,4)	3,023
H7N3	50,3 (0,6)	10,4199 (0,0006)	10,4199 (0,0006)	37,412 (0,002)	3217,8 (0,3)	3,075
H6N4	42,0 (0,6)	10,4113 (0,0007)	10,4113 (0,0007)	37,348 (0,003)	3505,9 (0,5)	3,085
H5N5	34,0 (0,7)	10,4045 (0,0008)	10,4045 (0,0008)	37,293 (0,004)	3496,2 (0,5)	3,094
H4N6	23,7 (0,8)	10,3975 (0,0009)	10,3975 (0,0009)	37,241 (0,005)	3486,7 (0,6)	3,102
H3N7	15,8 (0,7)	10,394 (0,001)	10,394 (0,001)	37,187 (0,009)	3479 (1)	3,109
H2N8	6,8 (0,4)	10,374 (0,002)	10,374 (0,002)	37,08 (0,01)	3456 (2)	3,124
H1N9	1,8 (0,5)	10,3646 (0,0000)	10,3646 (0,0000)	37,2388 (0,0000)	3464,426 (0,000)	3,122
H0N10	-	-	-	-	-	-
JCPDS *009-0169		10,4290*	10,4290*	37,3800*	3520,91*	3,07*

Table 5. Parameters obtained from the Fersmita phase refinement.

Phase: Fersmite -- $CaNb_2O_6$

System: Orthorhombic - Space Group: Pcan (60) -- α = β = γ = 90°

composite	mass (%)	*a*(Å)	*b*(Å)	*c*(Å)	V(Å^3)	ρ (g/cm^3)
H10N0	-	-	-	-	-	-
H9N1	0,9 (0,1)	15,079 (0,004)	5,860 (0,002)	5,072 (0,002)	448,1 (0,2)	4,771
H8N2	32,4 (0,5)	14,968 (0,001)	5,748 (0,001)	5,2151 (0,0003)	448,7 (0,1)	4,748
H7N3	41,6 (0,4)	14,967 (0,001)	5,7551 (0,0003)	5,2182 (0,0003)	449,48 (0,04)	4,757
H6N4	36,1 (0,3)	14,961 (0,001)	5,7528 (0,0003)	5,2178 (0,0003)	449,11 (0,05)	4,761
H5N5	33,4 (0,3)	14,962 (0,001)	5,7502 (0,0004)	5,2186 (0,0003)	448,97 (0,05)	4,762
H4N6	31,8 (0,4)	14,963 (0,001)	5,7470 (0,0003)	5,2183 (0,0003)	448,72 (0,04)	4,764
H3N7	30,9 (0,4)	14,970 (0,001)	5,7493 (0,0003)	5,2223 (0,0002)	449,46 (0,04)	4,757
H2N8	29,3 (0,3)	14,963 (0,001)	5,7422 (0,0003)	5,2181 (0,0002)	449,48 (0,04)	4,763
H1N9	23,9 (0,4)	14,970 (0,001)	5,748 (0,001)	5,224 (0,001)	449,45 (0,07)	4,757
H0N10	-	-	-	-	-	-
JCPDS *031-0289		15,0200*	5,7310*	5,2220*	449,51*	4,76*

Table 6. Parameters obtained from the refinement referring to dicalcium oxide diniobate phase.

Phase: Calcium Oxide Diniobate -- $Ca_2Nb_2O_7$

System: Orthorhombic - Space Group: Pn21a (33) -- α = β = γ = 90°

composite	mass (%)	*a* (Å)	*b* (Å)	*c*(Å)	V(Å^3)	ρ (g/cm^3)
H9N1	19,5 (0,2)	26,435 (0,002)	5,5003 (0,0003)	7,6862 (0,0004)	1117,6 (0,1)	4,493
JCPDS *070-2006		26,4570*	5,5010*	7,6920*	1119,49*	4,48*

Table 7. Parameters obtained from the refinement referring to the hydroxyapatite phase.

Phase: Hydroxyapatite -- HAp -- $Ca_{10}(PO_4)_6(OH)_2$

System: Hexagonal -Space Group: P63/m (176) -- α = β = 90° -- γ = 120°

composite	mass (%)	*a*(Å)	*b*(Å)	*c*(Å)	V(Å^3)	ρ (g/cm^3)
H10N0	96,6 (0,7)	9,4034 (0,0003)	9,4034 (0,0003)	6,8839 (0,0002)	527,15 (0,03)	3,165
H9N1	1,7 (0,2)	9,386 (0,002)	9,386 (0,002)	6,888 (0,002)	525,5 (0,3)	3,174

Continuation Table:

Phase: Hydroxyapatite -- HAp -- $Ca_{10}(PO_4)_6(OH)_2$

System: Hexagonal -Space Group: P63/m (176) -- α = β = 90° -- γ = 120°

composite	mass (%)	*a*(Å)	*b*(Å)	*c*(Å)	V($Å^3$)	ρ (g/cm^3)
JCPDS *009-0432		9,418*	9,418*	6,884*	528,800*	3,16*

Table 8. Parameters obtained from the refinement referring to niobium pentoxide phase.

Phase: Niobium Pentoxide -- Nb_2O_5

System: monoclínico-Space Group: P2(2) -- α = β = 90,000° -- γ = 119,804°

composite	mass (%)	*a*(Å)	*b* (Å)	*c* (Å)	V($Å^3$)	ρ (g/cm^3)
H0N10	100 (1)	21,157 (0,001)	3,824 (0,000)	19,357 (0,001)	1358,88 (0,11)	4,548
H1N9	16,2 (0,4)	21,143 (0,003)	3,826 (0,001)	19,334 (0,003)	1357,4 (0,3)	4,553
JCPDS *037-1468		20,381*	3,825*	19,368*	1360,55*	4,55

Table 9. Parameters obtained from the refinement referring to the phase of niobium phosphorus oxide.

Phase: Niobium Phosphorus Oxide -- PNb_9O_{25}

System: Tetragonal - Space Group: 14/m (87) -- α = β = γ = 90°

composite	mass (%)	*a* (Å)	*b*(Å)	*c*(Å)	V($Å^3$)	ρ (g/cm^3)
H10N0	-	-	-	-	-	-
H9N1	-	-	-	-	-	-
H8N2	-	-	-	-	-	-
H7N3	8,1 (0,2)	15,615 (0,001)	15,615 (0,001)	3,828 (0,001)	933,3 (0,1)	4,509
H6N4	22,0 (0,2)	15,607 (0,001)	15,607 (0,001)	3,8260 (0,0002)	931,9 (0,1)	4,516
H5N5	32,6 (0,3)	15,602 (0,001)	15,602 (0,001)	3,8255 (0,0002)	931,2 (0,1)	4,519
H4N6	44,6 (0,5)	15,600 (0,001)	15,600 (0,001)	3,8261 (0,0001)	931,1 (0,1)	4,519
H3N7	53,3 (0,5)	15,6085 (0,0003)	15,6085 (0,0003)	3,8279 (0,0001)	932,56 (0,04)	4,513
H2N8	63,9 (0,5)	15,610 (0,001)	15,610 (0,001)	3,8261 (0,0001)	933,3 (0,1)	4,509
H1N9	58,1 (0,7)	15,654 (0,001)	15,654 (0,001)	3,8259 (0,0003)	937,5 (0,1)	4,489
H0N10		-	-	-	-	-
JCPDS *081-1304		15,6390*	15,6390*	3,8317*	937,15*	4,49*

Table 10. Quantitative percentage mass fraction of the phases after the refinement by Rietveld.

	mass fraction (%)					
Sample	Phase (✳)	Phase (●)	Phase (♦)	Phase (+)	Phase (▼)	Phase (★)
H10N0	3,39	x	x	x	96,61	x
H9N1	77,88	0,9	x	19,48	1,74	x
H8N2	67,6	32,4	x	x	x	x
H7N3	50,33	41,59	8,09	x	x	x
H6N4	41,99	36,06	21,95	x	x	x
H5N5	34,05	33,4	32,55	x	x	x
H4N6	23,7	31,75	44,55	x	x	x
H3N7	15,77	30,91	53,32	x	x	x
H2N8	6,84	29,29	63,87	x	x	x
H1N9	1,77	23,88	58,12	x	x	16,23
H0N10	x	x	x	x	x	100

Legend: (✳) $Ca_3(PO_4)_2$; (●) $CaNb_2O_6$; (♦) PNb_9O_{25}; (+) $Ca_2Nb_2O_7$; (▼) $Ca_{10}(PO_4)_6(OH)_2$ and (★) (Nb_2O_5).

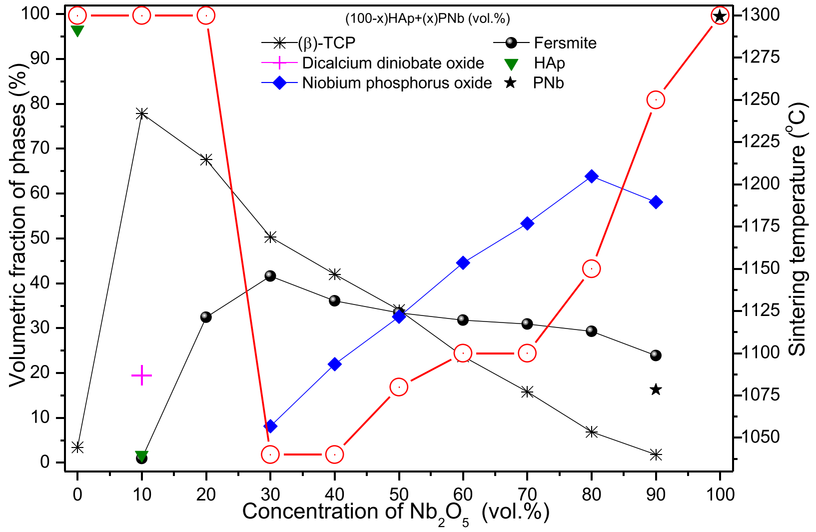

Figure 7. Analysis of the variation of the quantitative percentage mass fraction of the phases identified in the selected composites as a function of the PNb concentration and the sintering temperature. The line/symbol (--ʘ--) is only a visual guide to indicate the sintering temperatures.

3.3.3. Fourier Transform Infrared Photoacoustic Spectroscopy (FTIR-PAS)

Figure 8 shows the FTIR-PAS of the selected composites and also of the sintered hydroxyapatite and niobium pentoxide precursors at the temperatures that provided the highest degree of densification. For the H10N0 (HAp) sample, the characteristic hydroxyapatite bands are observed. In addition to these, bands at 1412 and 1486 cm^{-1} associated with CO_3^{2-} carbonate ions are also observed. Attenuation is observed in the intensity of the band corresponding to the vibration mode ν_L of OH$^-$ at 633 cm^{-1}, due to the dehydroxylation of HAp and indicates its decomposition at a temperature of 1300 °C, as observed in the XRD analysis. It is also observed, with the increase of PNb, attenuation and then disappearance of the vibrational bands related to the OH$^-$ functional group at 3571 and 633 cm^{-1}. In the spectra, two intense absorption regions are observed, one between 546 and 608 cm^{-1} and another in the range of 967-1120 cm^{-1}. These regions are characteristic of vibration modes ν_1 and ν_3, close to 1050 cm^{-1}, and ν_2, centered around 600 cm^{-1}, of functional group PO_4^{3-} and characteristic of HAp and β-TCP phases.

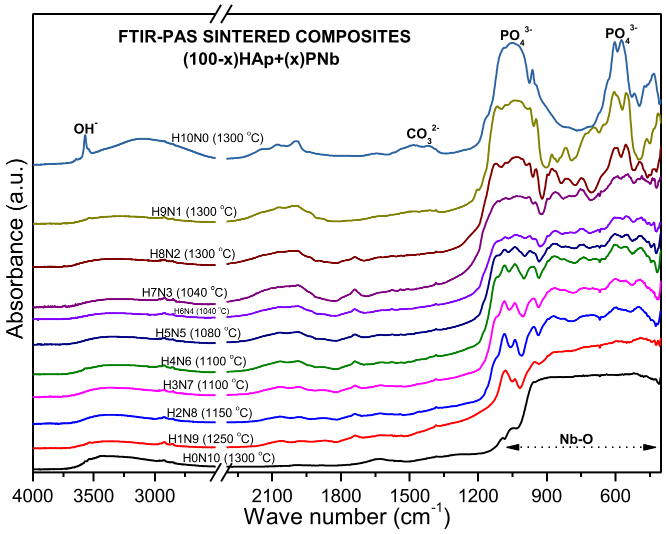

Figure 8. Infrared vibrational spectra (FTIR-PAS) for the selected composites and precursors HAp and PNb in the respective sintering temperatures.

The intensity of these vibrations, in the considered regions, decreases with the increase of the PNb concentration and it is observed the appearance of other bands, associated with the phasesof the sintering process of the composites. In the range between 400 and 950 cm-1, vibrational bands related to the elongation of the Nb-O bond, the angular deformation of the Nb-O-Nb bond and the elongation of the Ca-O bond are observed, characteristics of $CaNb_2O_6$, $Ca_2Nb_2O_7$, PNb_9O_{25} and Nb_2O_5 [27–29]. In general, a great overlap of these vibrational bands is observed both in terms of temperature and concentration, notably in the region between 400 and 1130 cm^{-1}. For a more careful analysis of these overlaps, it would be necessary to use the deconvolution curve fitting methodology to investigate and identify linkage changes and other factors such as stretching and deformation [30,31].

3.3.4. Raman spectroscopy analysis

The bands observed in **Figure 9(A-K)** show the Raman spectra of the selected composites and also the HAp and PNb precursors. For the (▼) HAp phase, **Figure 9(A)** shows an intense band at 962 cm^{-1} (ν_1) and bands associated with vibration modes ν_2 at 432 and 448 cm^{-1}, ν_3 at 1029.5, 1048,5 and 1077 cm^{-1} and ν_4 at 582, 593 and 609 cm^{-1}, related to the characteristics of PO_4^{3-} ion and hydroxyapatite. The Raman spectrum, **Figure 9(K)**, corresponds to the phase (★) PNb. The bands observed in the range from 850 to 1000 cm^{-1} are attributed to the Nb=O terminal stretching mode, while those observed in the region between 440 and 800 cm^{-1} correspond to bands from the symmetric drawing mode of the PNb polyhedron, and those in the range between 200 and 350 cm^{-1} they are associated with the angular deformation mode of Nb-O-Nb[32,33].

In the spectra shown in **Figure 9(B to J)**, the characteristic bands of the HAp and PNb phases are not observed, indicating the decomposition of these phases. For the composite H9N1, sintered at 1300 °C, the characteristic bands of phase (*) β-TCP at 971.5 and 951 cm^{-1}, of (+) dicalcium diniobate oxide at 843, 748, 627, 581, 348, 315 and 241 cm^{-1} and a low-intensity peak at 904 cm^{-1} which is associated with the fersmite phase (●). The (+) dicalcium diniobate oxide phase was detected only for the H9N1 composition, according to the result obtained by X-ray diffraction. From the H8N2 to H1N9 composition, there is a decrease in the intensity of the phase bands (*) β-TCP and an increase in the intensity of the bands related to the phase (●) fersmite at 904, 848, 539, 496, and 292 cm^{-1}, associated with vibrations of the Nb-O type, whose intensities decrease with the increase in the concentration of PNb[34]. The phase (♦) of niobium phosphorus oxide is observed from the H8N2 sample with bands located at 1010, 627, 694 cm^{-1}. These bands increase in intensity with increasing amount of niobium pentoxide. In general, it can be seen that for all composites, the bands of the fersmite phase are more intense for the highest concentrations of HAp, while for the highest concentrations of PNb, the phase of niobium phosphorus oxide (PNb_9O_{25}) is the more evident. The results obtained by Raman spectroscopy for the analyzed composites are consistent with the results obtained by XRD.

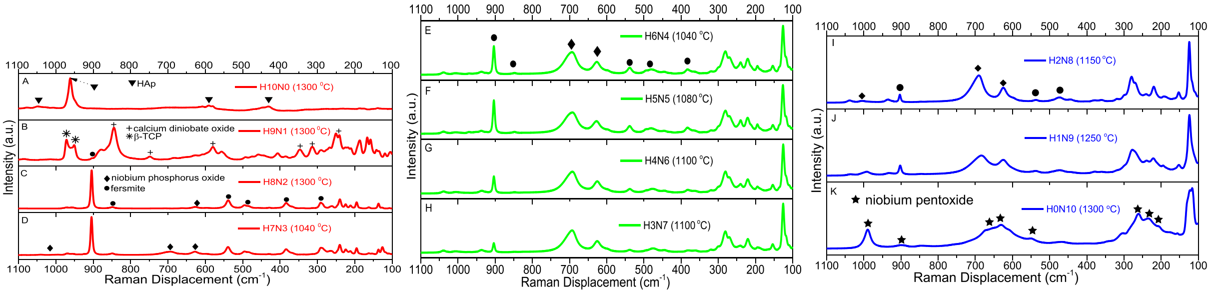

Figure 9 (A-K). Raman spectra related to the selected composites and the precursors HAp and PNb in the respective sintering temperatures.

3.3.5. Scanning electron microscopy (SEM) analysis

The surface and fracture micrographs obtained by SEM of the selected composites (100-x)HAp+(x) PNb, with x = 10, 20, 30, 40, 50, 60, 70, 80 and 90 (vol. %) of the HAp and PNb precursors are shown in **Figure 10**. A significant microstructural variation (see surface **Figure 10**) is observed in the analysis of surface micrographs of the composites. In the H9N1 and H8N2 composites, an estimated grain size between 2 and 8 μm is observed, and the grain morphology of the H8N2 composite has a more rounded appearance than that of the H9N1, and both have low porosity. The HAp precursor, sintered at 1300 ℃, also presents low porosity and has a microstructure composed of equiaxed grains with estimated sizes between 1 and 25 μm. The microstructure observed in intermediate composites from H7N3 to H3N7 is quite complex. Concerning grain size, a significant decrease is observed for the H7N3 composition, with an estimated size smaller than 3 μm and more uniform morphology. For compositions H6N4 and H5N5, there is an increase in grain size with heterogeneous morphology and a low degree of porosity. In the composition of H4N6, an increase in the estimated grain size is observed, varying between approximately 1 and 8 μm, with varied and quite heterogeneous morphology different from those observed previously. For composites H3N7, H2N8 and H1N9, with higher PNb content, there is a significant change in the microstructure of the composites, observing morphological structures (grains) with a more elongated shape in the form of rods. In the surface micrograph of PNb sintered at 1300 ℃, grains in cylindrical and spherical shapes, with estimated sizes varying between 3 and 15 μm, are visible. The fracture surfaces shown in **Figure 10** show a certain degree of porosity, to a greater or lesser extent depending on the composition. Pores with estimated sizes of around 0.5 to 8 μm are observed. HAp has low porosity with pores located at the grain boundaries while niobium pentoxide has a higher degree of porosity with pores of up to 10 μm. It is also observed, for all composites, the occurrence of intergranular fracture, that is, along the contours of the grains, characteristic of ceramic materials. The microstructures of the selected composites are highly complex in the morphological aspects due to the composition, the sintering temperature, the presence of two or more phases with different structures, and the occurrence of sintering in liquid phase in some composites. X-ray diffraction analysis as a function of temperature can be of great value to study the formation of detected phases and identifying the phase that induces sintering by the liquid phase.

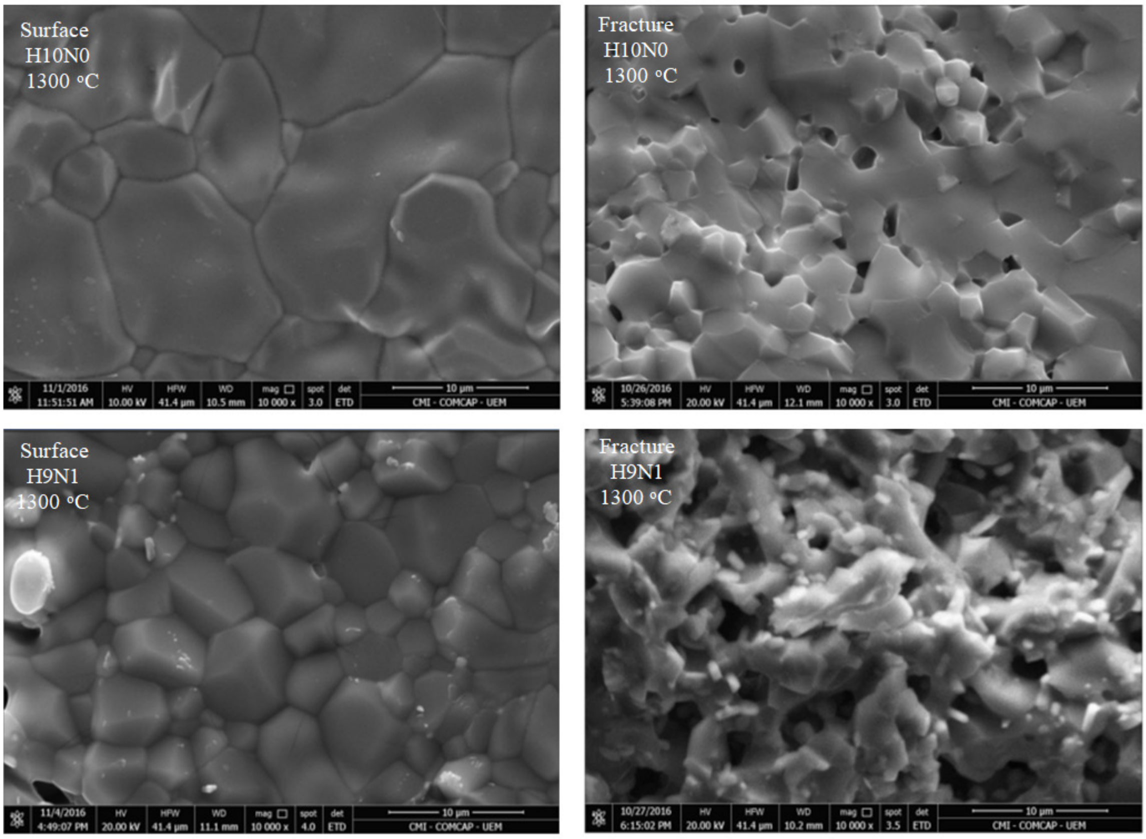

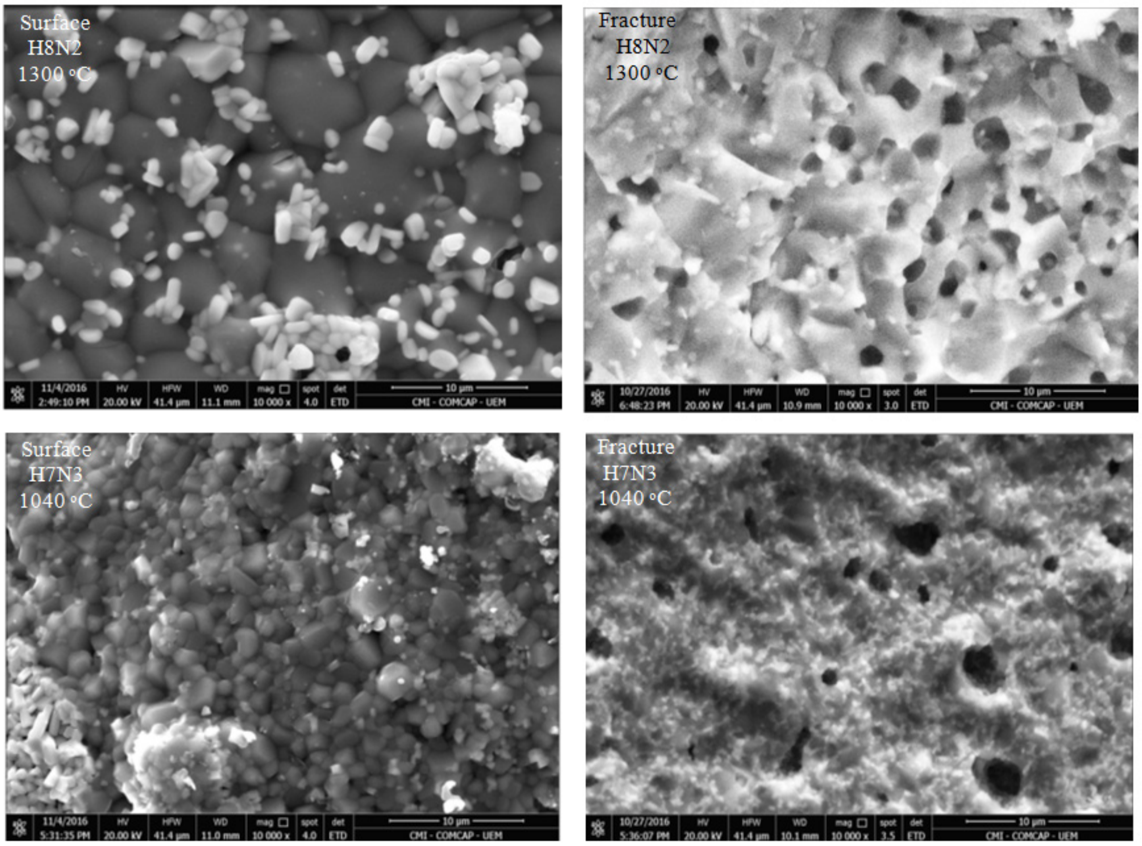

Figure 10. Surface SEM and fracture micrographs for selected composites and precursors.

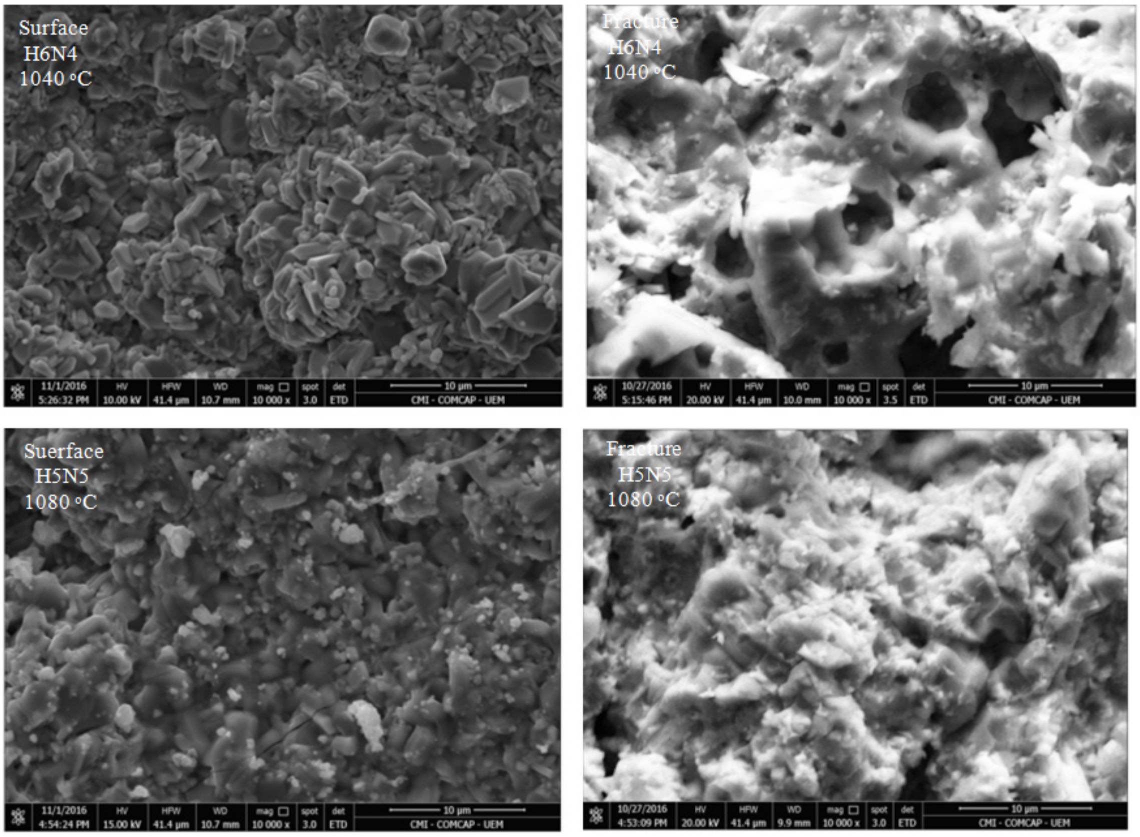

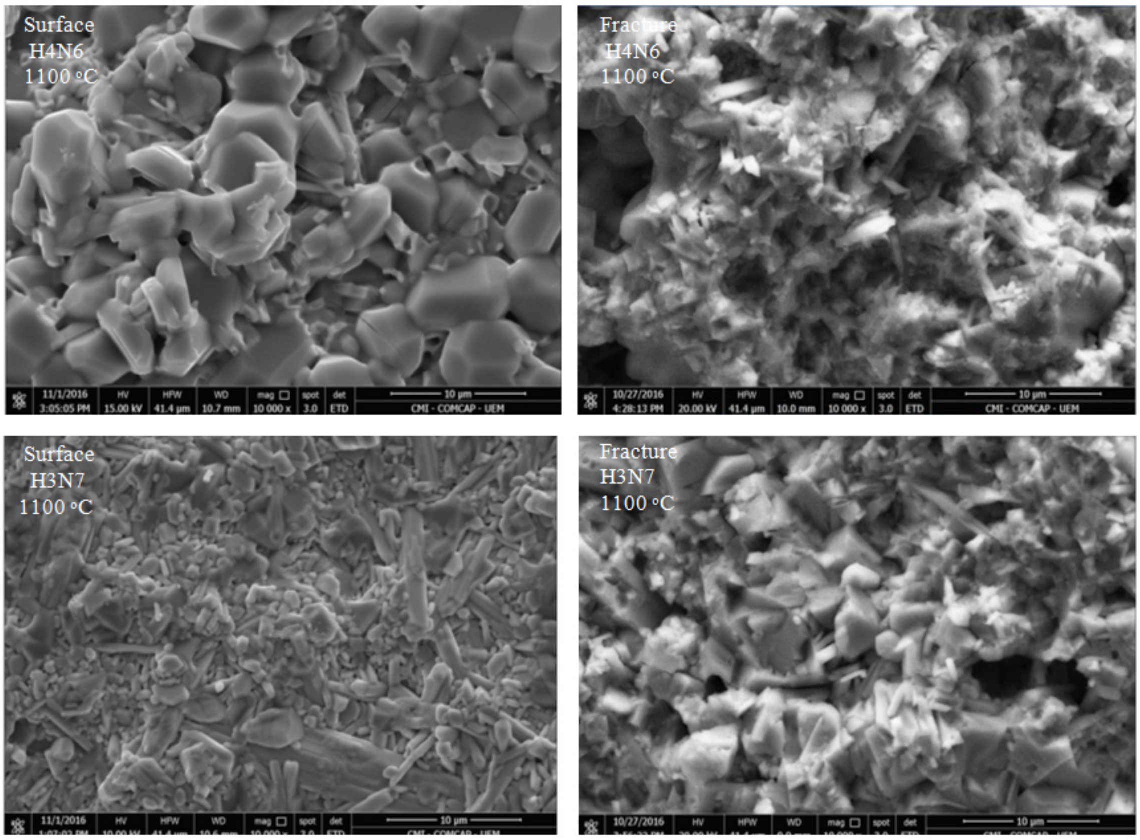

Figure 10. (cont.) Surface and fracture SEM micrographs for the nine (9) selected composites and two (2) precursors.

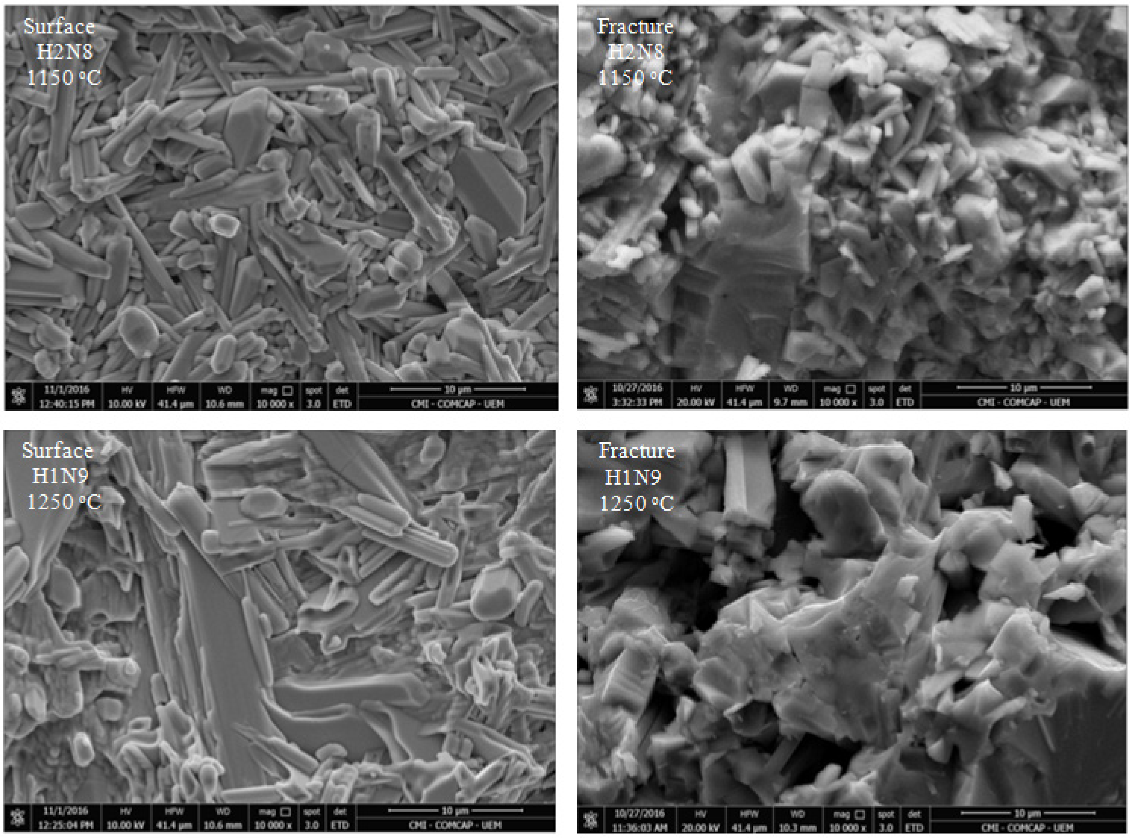

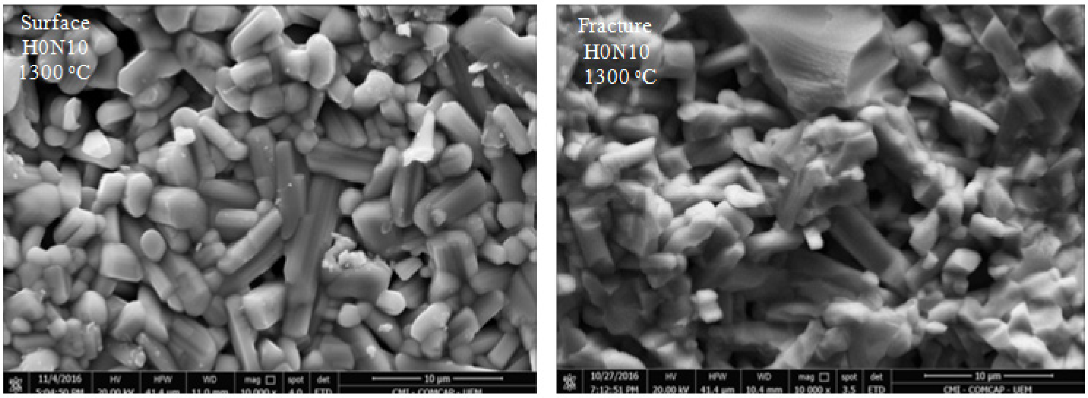

Figure 10. (cont.) Surface and fracture SEM micrographs for the nine (9) selected composites and two precursors (2).

3.3.6. Semiquantitative chemical analysis by energy dispersive X-rays (EDS)

Semi-quantitative X-ray energy dispersive (EDS) chemical analysis of selected composites and precursors is shown in **Figure 11(A-H)** and **(I-K)**. The region in which the analysis was performed corresponds, for all samples, to the corresponding surface micrograph area. The main chemical elements identified were Ca, P and Nb and in smaller amounts, Mg and Na, and their percentage values (% by mass) are presented in **Figure 11(A-K)**. The elements Mg and Na in the observed amounts are generally found in bones after calcination. The percentage amount (% by mass) of the elements Ca, P and Nb varies according to the concentration of HAp and PNb in the composite, as seen in **Figure 12**. Note that with the increase in the concentration of PNb, there is a decrease (linear) for the Ca and P elements, while for the Nb element, there is an increase (linear). This linear behavior is by the methodology used to prepare the composites, the mixing rule.

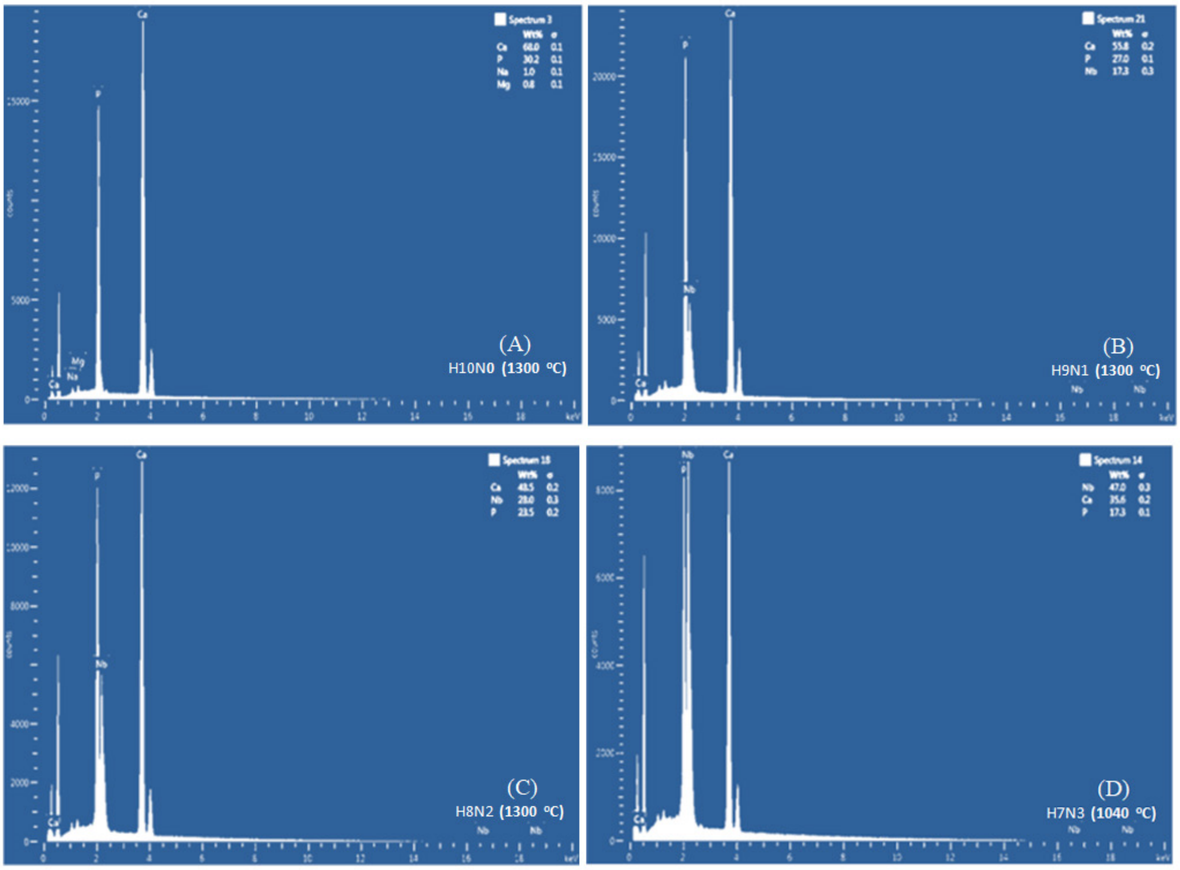

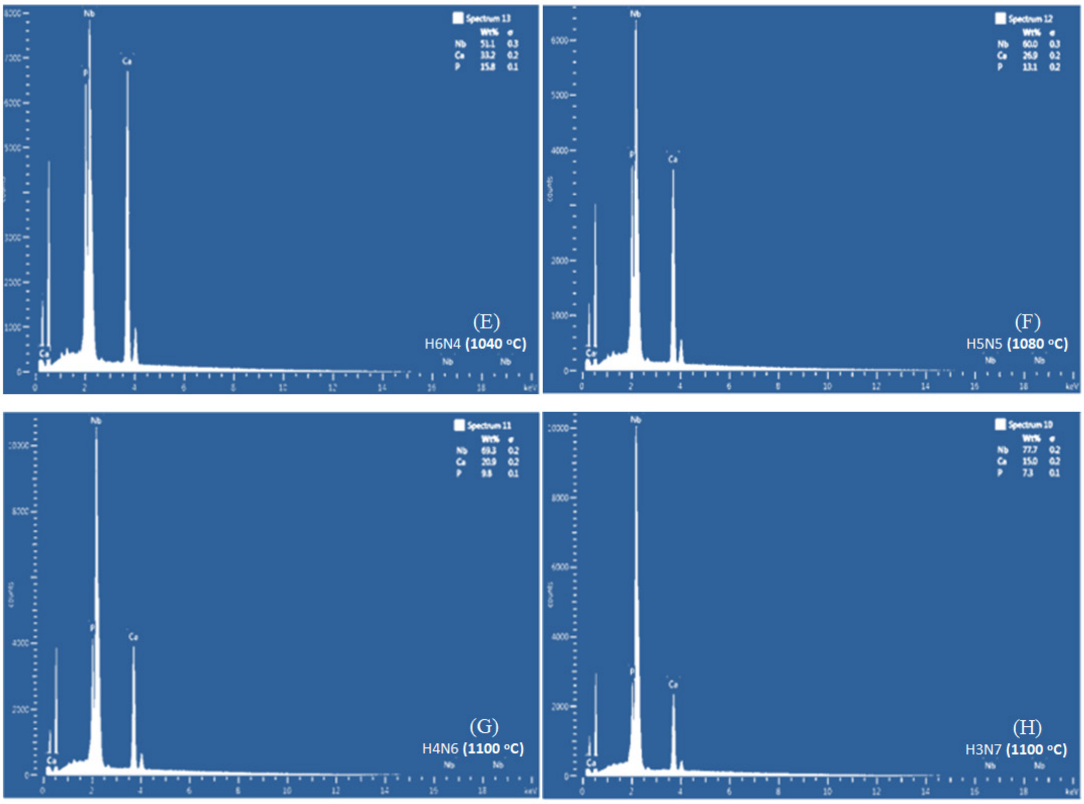

Figure 11 (A-H). Analysis by EDS's performed on the surface of the samples of HAp, and of PNb and of the nine (9) selected composites.

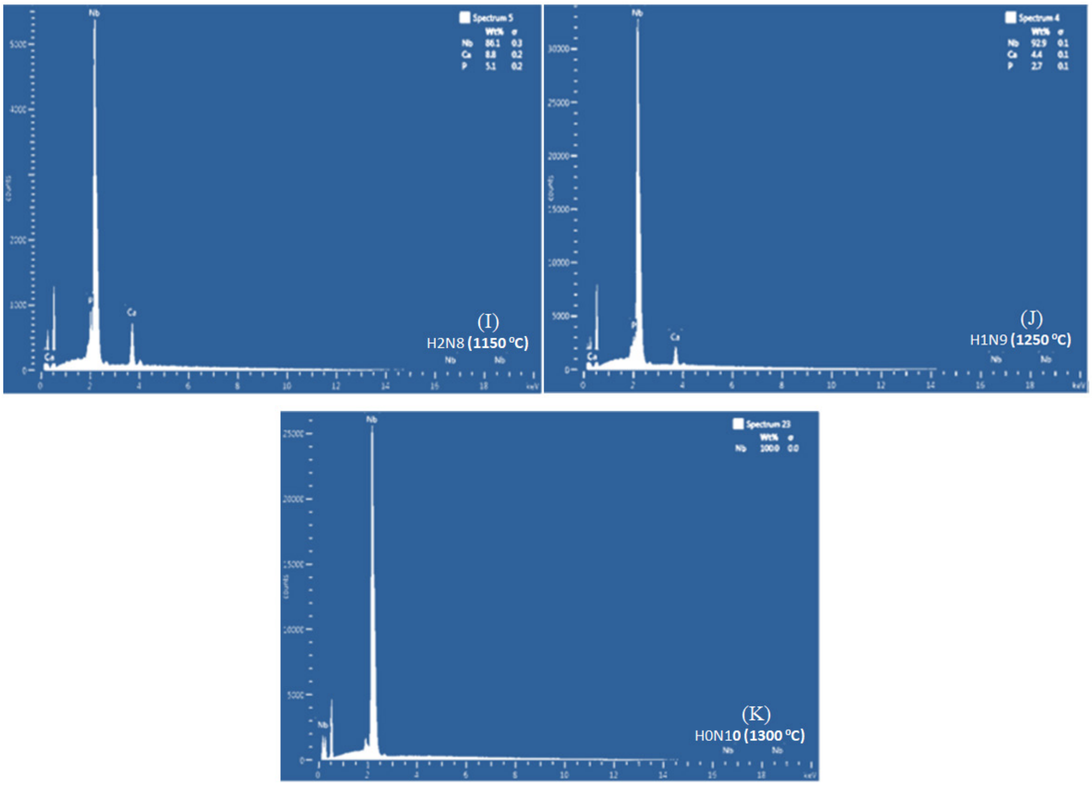

Figure 11 (I-K). (cont.) Analyzes by EDS's performed on the surface of the samples of HAp, PNb and the nine (9) selected composites.

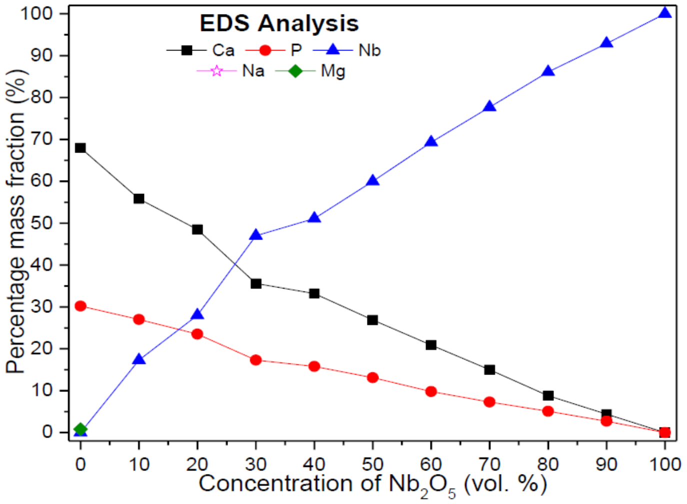

Figure 12. Percentage change of the chemical elements obtained by semiquantitative analysis (EDS) for the selected composites as a function of the PNb concentration.

The results of the Ca/P molar ratio for compositions with $x \neq 0$ are also shown in **Table 11** and, when compared with data found in the literature[2], for the β-TCP phase with a molar ratio of 1.50, a variation of the order of 6% for x values between 10 and 70% and the other two compositions, a more significant deviation. For a better evaluation of the percentage of chemical elements in the composites, the analysis by EDS must be carried out in a larger sample, that is, in several regions of the sample to obtain a more representative average value and also to perform quantitative chemical analysis by Emission Spectrometry Plasma Optics (ICP) or Atomic Absorption Spectrophotometry (AAS).

Table 11. Results of semiquantitative chemical analysis by EDS.

Sample	Temp. (°C)	Chemical elements (mass %)					Molar ratio Ca/P
		Ca	P	Nb	Na	Mg	
H10N0	1300	68,0±0,1	30,2±0,1	x	1,0±0,1	0,8±0,1	x
H9N1	1300	55,8±0,2	27,0±0,1	17,3±0,3	x	x	1,591
H8N2	1300	48,5±0,2	23,5±02	28,0±0,3	x	x	1,595
H7N3	1040	35,6±0,2	17,3±0,1	47,0±0,3	x	x	1,590
H6N4	1040	33,2±0,2	16,1±0,1	51,1±0,3	x	x	1,594
H5N5	1080	26,9±0,2	13,1±0,2	60,0±0,3	x	x	1,588
H4N6	1100	20,9±0,2	10,19±0,1	69,3±0,2	x	x	1,585
H3N7	1100	15,0±0,2	7,3±0,1	77,7±0,2	x	x	1,588
H2N8	1150	8,8±0,2	5,1±0,2	86,1±0,3	x	x	1,337
H1N9	1250	4,4±0,1	2,7±0,1	92,9±0,1	x	x	1,259
H0N10	1300	x	x	100,0±0,0	x	x	x

3.3.7. Stoichiometric equations for chemical reactions

In this topic, we will consider the chemical and solid-state reactions that produce the decomposition of HAp and PNb, depending on the composition and sintering temperature, for the selected composites and also for the precursor materials. The reactions that occur are the result of the interaction between hydroxyapatite [HAp, $Ca_{10}(PO_4)_6(OH)_2$] and niobium pentoxide [PNb, Nb_2O_5], in an air atmosphere, which induce the decomposition of these two phases and the appearance of others. The different reactions that can occur in the materials studied are associated with the increase in temperature and the release of water vapor, with partial or total loss of the OH^- radical from HAp [35], associated with oxidation and decomposition processes and the formation of new ones phases. The decomposition of HAp occurs by the loss of the OH^- radical and formation of the $Ca_3(PO_4)_2$ phase, leaving the reaction of CaO (excess), which reacts with niobium pentoxide, forming the $Ca_2Nb_2O_7$ and $CaNb_2O_6$ phases. These phases were detected by XRD techniques and confirmed by Raman spectroscopy, at a temperature of 700 °C (the lowest temperature used in this work), and subsequently, with the increase in PNb concentration and temperature, the formation of the PNb_9O_{25} phase occurs. It is observed that for composites H7N3, H6N4, H5N5, H4N6, H3N7 and H2N8 the same chemical reactions occur, differing only by their participation in % by volume, as can be seen in the results that appear in the tables after refinement. The equations of the chemical reactions that can lead to the formation of these phases are presented.

H10N0

$$\mathbf{Ca_{10}(PO_4)_6(OH)_2} \rightarrow 3Ca_3(PO_4)_2 + CaO + H_2O$$

H9N1

$$\mathbf{Ca_{10}(PO_4)_6(OH)_2} \rightarrow 3Ca_3(PO_4)_2 + CaO + H_2O$$
$$CaO + Nb_2O_5 \rightarrow \mathbf{CaNb_2O_6}$$
$$CaNb_2O_6 + CaO \rightarrow \mathbf{Ca_2Nb_2O_7}$$

H8N2

$$Ca_{10}(PO_4)_6(OH)_2 \rightarrow 3\mathbf{Ca_3(PO_4)_2} + CaO + H_2O$$
$$CaO + Nb_2O_5 \rightarrow \mathbf{CaNb_2O_6}$$

H7N3, H6N4, H5N5, H4N6, H3N7, H2N8

$$Ca_{10}(PO_4)_6(OH)_2 \rightarrow 3\mathbf{Ca_3(PO_4)_2} + CaO + H_2O$$
$$CaO + Nb_2O_5 \rightarrow \mathbf{CaNb_2O_6}$$
$$Ca_3(PO_4)_2 + 9Nb_2O_5 \rightarrow \mathbf{PNb_9O_{25}} + 3CaO$$

H1N9

$$Ca_{10}(PO_4)_6(OH)_2 \rightarrow 3\mathbf{Ca_3(PO_4)_2} + CaO + H_2O$$
$$CaO + Nb_2O_5 \rightarrow \mathbf{CaNb_2O_6}$$
$$Ca_3(PO_4)_2 + 9Nb_2O_5 \rightarrow 2\mathbf{PNb_9O_{25}} + 3CaO$$
$$Nb_2O_5 \rightarrow \mathbf{Nb_2O_5}$$

H0N10

$$Nb_2O_5 \rightarrow \mathbf{Nb_2O_5}$$

3.3.8. Vickers microhardness (VH)

Figure 13 shows the results of the Vickers Hardness (VH) values as a function of the PNb concentration and the sintering temperature, for the selected composites that presented the best densifications, among those studied. It is observed, for the precursors HAp and PNb, both sintered at 1300 °C, hardness values of 4.17 and 3.52 GPa, respectively. For composites with x = 10, 20, 30, 40, 50, 60, 70, 80 and 90 (vol%), both the composition and the sintering temperature would influence the hardness values. The lowest hardness value of 2.04 GPa occurs for the H8N2 composition sintered at 1300 °C, and the highest hardness value of 3.73 GPa was observed for the H4N6 composition sintered at a temperature of 1100 °C. These hardness values are higher than those reported for sintered hydroxyapatite at temperatures of 1050 and 1100 °C, of 1.1 and 1.35 GPa, respectively. A comparative analysis allows concluding that the use of niobium pentoxide produces an improvement in the microhardness properties in relation to the HAp matrix, being able to reach higher values, in the order of three times, in relation to HAp sintered at the same temperature[15,36].

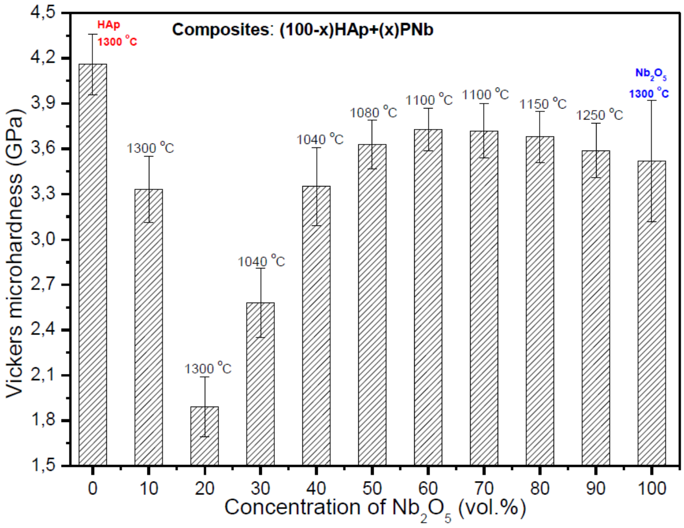

Figure 13. Vickers hardness (HV) values as a function of the PNb concentration and the sintering temperature for the selected composites and also the precursors. The solid line is just a visual guide (spline).

4. Conclusion

The percentage volume of PNb induces in composites, mainly in the range of 1040 to 1150 °C, a reduction in the beginning of the melting point, allowing them to be sintered at lower temperatures, which provides a lower production cost in terms of energy and an improvement on physical properties and Vickers hardness. The thermal treatment and concentration of the HAp/PNb composite, at the temperatures used, induces the loss of the OH^- functional group of HAp, and the reactions that occur in the process between hydroxyapatite and niobium pentoxide result in composites formed by the phases: β-tricalcium phosphate ($Ca_3(PO_4)_2$; niobium phosphorus oxide (PNb_9O_{25}); niobium calcium oxide ($CaNb_2O_6$) and dicalcium diniobate oxide ($Ca_2Nb_2O_7$), whose mass fractions (%) depend on composition and temperature. The physical properties and Vickers microhardness of the composites produced have a high degree of dependence on both the concentration and the sintering temperature. The H4N6 composition, sintered at 1100 °C, showed the best values for physical properties, that is, the highest linear contraction (~9.75%), the highest density (~3.85 g/cm^3) and the lowest porosity (~4.00%) and that these properties practically do not vary between temperatures 1040 and 1100 °C. Of the investigated compositions, the intermediates H7N3 H6N4, H5N5, H4N6 and H3N7 are the ones that present a significant reduction in the onset of the melting point compared to the precursor materials, possibly due to the occurrence of sintering with the liquid phase, obtaining values for the density and hardness in lower temperatures. Finally, it is concluded that the analysis techniques used showed that the high energy milling and powder metallurgy techniques followed by the production of the HAp/PNb composite in bulk as a function of the sintering concentration and temperature were efficient, indicating that they can be used for future applications in medicine and/or dentistry.

5. Acknowledgements

We extend our gratitude to DFI/UEM, DQI/UEM, DZO/UEM, COMCAP/UEM, CBMM, CAPES, CNPq, FINEP, and Araucária Foundation for providing the financial support for this project. A special thanks to the educators: Antonio Medina Neto, Walter Moreira Lima, and Wilson Ricardo Weinand (in memoriam).

References

[1] Joon B. Park RSL. Biomaterials [Internet]. New York, NY: Springer New York; 2007. XII, 562. Available from: http://link.springer.com/10.1007/978-0-387-37880-0

[2] Dorozhkin S. Medical Application of Calcium Orthophosphate Bioceramics. BIO [Internet]. 2011 Feb 21;1(1):1–51. Available from: http://www.ccaasmag.org/bio_2011/vol1/Dorozhkin-CaPO$_4$-bioceramics.pdf

[3] Nascimento WJ, Bonadio TGM, Freitas VF, Weinand WR, Baesso ML, Lima WM. Nanostructured Nb_2O_5–natural hydroxyapatite formed by the mechanical alloying method: A bulk composite. Mater Chem Phys [Internet]. 2011 Oct;130(1–2):84–9. Available from: https://linkinghub.elsevier.com/retrieve/pii/S0254058411004755

[4] RMF Sousa, LE Fernandes WG. Nióbio. Química Nova na Escola. 2013;35:68–9.

[5] Mariucci VVG, da Cruz JA, Bonadio TGM, Picolloto AM, Weinand WR, Lima WM, et al. Effective Thermal Diffusivity Study of Powder Biocomposites via Photoacoustic Method. Brazilian Journal of Physics [Internet]. 2015 Oct 21;45(5):525–31. Available from: http://link.springer.com/10.1007/s13538-015-0344-9

[6] Johansson CB, Albrektsson T. A removal torque and histomorphometric study of commercially pure niobium and titanium implants in rabbit bone. Clin Oral Implants Res [Internet]. 1991 Jan 23; 2 (1): 24–9. Available from: https://onlinelibrary.wiley.com/doi/10.1034/j.1600-0501.1991.020103.x

[7] Tamai M, Isama K, Nakaoka R, Tsuchiya T. Synthesis of a novel b-tricalcium phosphate/hydroxyapatite biphasic calcium phosphate containing niobium ions and evaluation of its osteogenic properties. J Artif Organs [Internet]. 2007 Mar 23;10(1):22–8. Available from: http://link.springer.com/10.1007/s10047-006-0363-y

[8] Fathi MH, Salehi M, Mortazavi V, Mousavi SB, Parsapour A. Novel hydroxyapatite/niobium

surface coating for endodontic dental implant. Surf Eng [Internet]. 2006 Oct 1;22(5):353–8. Available from: http://journals.sagepub.com/doi/10.1179/174329406X126708

[9] Prado da Silva MH, Monteiro AM, Neto JAC, Morais SMO, dos Santos FFP. Nano-Sized Apatite Coatings on Niobium Substrates. Key Eng Mater [Internet]. 2003 Dec;254–256:439–42. Available from: https://www.scientific.net/KEM.254-256.439

[10] Musetti, H. C.; Neves Junior, L. F.; Santos, M. F. Paris EC. Uso de nanopartículas de hidroxiapatita pura e impregnadas com Nb_2O_5 para aplicações em fotocatálise. In: Embrapa Instrumentação. 2013. p. 436–8.

[11] Lima WM, Weinand WR, Biondo V, Nogueira ES, Medina AN, Baesso ML, et al. Microstructure effects on the thermal properties of vacuum sintered AISI 316L stainless steel. Rev Sci Instrum [Internet]. 2003 Jan 1;74(1):716–8. Available from: https://pubs.aip.org/rsi/article/74/1/716/1068100/Microstructure-effects-on-the-thermal-properties

[12] Lima CJ de, Silva IIC da, Barros LFH de, Graneiro JM, Silva MHP da. Resposta do tecido subcutâneo de camundongos à implantação de um novo biovidro à base de óxido de nióbio. Matéria (Rio Janeiro) [Internet]. 2011;16(1):574–82. Available from: http://www.scielo.br/scielo.php?script=sci_arttext&pid=S1517-70762011000100004&lng=pt&tlng=pt

[13] Pauline SA, Rajendran N. Biomimetic novel nanoporous niobium oxide coating for orthopaedic applications. Appl Surf Sci [Internet]. 2014 Jan;290:448–57. Available from: https://linkinghub.elsevier.com/retrieve/pii/S0169433213021909

[14] Demirkol N, Oktar FN, Kayali ES. Mechanical and Microstructural Properties of Sheep Hydroxyapatite (SHA)-Niobium Oxide Composites. Acta Phys Pol A [Internet]. 2012 Jan;121(1):274–6. Available from: http://przyrbwn.icm.edu.pl/APP/PDF/121/a121z1p85.pdf

[15] Demirkol N, Meydanoglu O, Gökçe H, Oktar FN, Kayali ES. Comparison of Mechanical Properties of Sheep Hydroxyapatite (SHA) and Commercial Synthetic Hydroxyapatite (CSHA)-MgO Composites. Key Eng Mater [Internet]. 2011 Oct;493–494:588–93. Available from: https://www.scientific.net/KEM.493-494.588

[16] Demirkol N, Oktar FN, Kayali ES. Influence of Niobium Oxide on the Mechanical Properties of Hydroxyapatite. Key Eng Mater [Internet]. 2012 Nov 29;529–530:29–33. Available from: https://www.scientific.net/KEM.529-530.29

[17] da Cruz JA, Weinand WR, Neto AM, Palácios RS, Sales AJM, Prezas PR, et al. Low-Cost Hydroxyapatite Powders from Tilapia Fish. JOM [Internet]. 2020 Apr 22;72(4):1435–42. Available from: http://link.springer.com/10.1007/s11837-019-03998-4

[18] Wilson Ricardo Weinand and Walter Moreira Lima. Produção de Hidroxiapatita Via Calcinação de Osso de Peixe. 2017, Patent PI 0506242.

[19] Nico C, Monteiro T, Graça MPF. Niobium oxides and niobates physical properties: Review and prospects. Prog Mater Sci [Internet]. 2016 Jul;80:1–37. Available from: https://linkinghub.elsevier.com/retrieve/pii/S0079642516000116

[20] da Cruz JA, Volnistem EA, Ferreira RF, Freitas DB, Sales AJM, Costa LC, et al. Structural characterization of Brazilian niobium pentoxide and treatment to obtain the single phase ($H-Nb_2O_5$). Therm Sci Eng Prog [Internet]. 2021 Oct;25:101015. Available from: https://linkinghub.elsevier.com/retrieve/pii/S2451904921001761

[21] Vicente Chiaverini. Metalurgia do Pó Técnica e Produtos. Sao paulo: ABM - Associação Brasileira de Metais; 1982. 272 p.

[22] Suryanarayana C. Mechanical alloying and milling. Prog Mater Sci. 2001 Jan 1;46(1–2):1–184.

[23] Standard Test Method for Water Absorption, Bulk Density, Apparent Porosity, and Apparent Specific Gravity of Fired Whiteware Products [Internet]. [cited 2024 Sep 8]. Available from: https://www.astm.org/c0373-88r99.html

[24] de Oro Calderon R, Gierl-Mayer C, Danninger

H. Fundamentals of Sintering: Liquid Phase Sintering. In: Encyclopedia of Materials: Metals and Alloys [Internet]. Elsevier; 2022. p. 481–92. Available from: https://linkinghub.elsevier.com/retrieve/pii/B9780128197264001277

[25] Casa Grande HL. Curso Introdutório ao método Rietveld. Maringá; 2007.

[26] Mathai KC, Vidya S, John A, Solomon S, Thomas JK. Structural, Optical, and Compactness Characteristics of Nanocrystalline $CaNb_2O_6$ Synthesized through an Autoigniting Combustion Method. Adv Condens Matter Phys [Internet]. 2014;2014:1–6. Available from: http://www.hindawi.com/journals/acmp/2014/735878/

[27] Haris PI. Advances in Biomedical Spectroscopy, 2012.

[28] Li C, Xiang H, Qin Y, Fang L. Effects of barium substitution on the sintering behavior, dielectric properties of $Ca_2Nb_2O_7$ ferroelectric ceramics. J Adv Dielectr [Internet]. 2017 Apr 3; 07 (02): 1750013. Available from: https://www.worldscientific.com/doi/abs/10.1142/S2010135X17500138

[29] Zhou J, Feng G, Li L, Huang F, Shen H, Yang H, et al. In situ Raman spectroscopy and X-ray diffraction of pressure-induced phase transition in columbite $CaNb_2O$. J Alloys Compd [Internet]. 2013 Dec; 579: 267–71. Available from: https://linkinghub.elsevier.com/retrieve/pii/S0925838813014515

[30] Husson E, Repelin Y, Dao NQ, Brusset H. Normal coordinate analysis for $CaNb_2O_6$ of columbite structure. J Chem Phys [Internet]. 1977 Jun 1;66(11):5173–80. Available from: https://pubs.aip.org/jcp/article/66/11/5173/774726/Normal-coordinate-analysis-for-CaNb2O6-of

[31] Walters MA, Leung YC, Blumenthal NC, Konsker KA, LeGeros RZ. A Raman and infrared spectroscopic investigation of biological hydroxyapatite. J Inorg Biochem [Internet]. 1990 Jul; 39 (3): 193–200. Available from: https://linkinghub.elsevier.com/retrieve/pii/0162013490840027

[32] Berzina-Cimdina L, Borodajenko N. Research of Calcium Phosphates Using Fourier Transform Infrared Spectroscopy. In: Infrared Spectroscopy - Materials Science, Engineering and Technology. 2012.

[33] Ristić M, Popović S, Musić S. Sol–gel synthesis and characterization of Nb_2O_5 powders. Mater Lett [Internet]. 2004 Aug; 58 (21): 2658–63. Available from: https://linkinghub.elsevier.com/retrieve/pii/S0167577X04002472

[34] Brejão AS, Morais MO, Vendrametto O. Tendências para o uso de nióbio no setor de microeletrônica. Clean Prod Towar A Sustain Transit. 2015;5:1–10.

[35] Callister Jr WD. Materials science and engineering – An introduction. [Internet]. Vol. 45, Materials and Corrosion. 1994. 632–633 p. Available from: https://onlinelibrary.wiley.com/doi/10.1002/maco.19940451110

[36] Callister Jr WD, Rethwisch DG. Materials science and engineering: an introduction. John wiley & sons; 2020.